~~High-resolution~~ 1 km all-sky ~~land surface temperature and~~ net radiation over Europe enabled by the merging of land surface temperature retrievals from geostationary and polar-orbiting satellites.

Dominik Rains[1], Isabel Trigo[2], Emanuel Dutra[2], Sofia Ermida[2], Darren Ghent[3], Petra Hulsman[1], Jose Gómez-Dans[4], and Diego G. Miralles[1]

[1]Hydro-Climate Extremes Lab (H-CEL), Ghent University, Ghent, Belgium
[2]Instituto Português do Mar e da Atmosfera, Lisboa, Portugal
[3]University of Leicester, Space Research Centre, Leicester, United Kingdom
[4]University College London, Gower Street, London, United Kingdom

Correspondence: Dominik Rains (dominik.rains@airbus.com)

Abstract. ~~Land Surface Temperature (LST) and Surface~~ Surface Net Radiation (SNR) ~~are vital inputs~~ is a vital input for many land surface and hydrological models. However, current remote sensing datasets of ~~these variables~~ SNR come mostly at coarse resolutions ~~. Although high-resolution LST and SNR retrievals are available, they~~ or have large gaps due to cloud-cover that hinder their use as input in models. Here, we present a downscaled and continuous daily ~~LST and~~ SNR product across Europe for 2018–2019. ~~The~~ Longwave outgoing radiation is computed from a merged land surface temperature (LST) product in combination with Meteosat Second Generation (MSG) emissivity data. The merged LST product is based on all-sky LST retrievals from the Spinning Enhanced Visible and InfraRed Imager (SEVIRI) onboard the geostationary Meteosat Second Generation (MSG) satellite, and clear-sky LST retrievals from the Sea and Land Surface Temperature Radiometer (SLSTR) onboard the polar-orbiting Sentinel 3 satellites. ~~The product combines~~ This approach makes use of the medium spatial (approx. 5–7 km) but high temporal (30 minute) resolution, gap-free data from MSG, with the low temporal (2–3 days) but high spatial (1 km) resolution of the Sentinel 3 LST retrievals. The resulting 1 km and daily LST dataset is based on an hourly merging of both datasets through bias-correction and Kalman Filter assimilation. ~~Longwave outgoing radiation is computed from the merged LST product in combination with MSG-based emissivity data.~~ Shortwave outgoing radiation is computed from the incoming shortwave radiation from MSG and downscaled ~~albedos~~ albedo using 1 km PROBA-V data. MSG incoming shortwave and longwave radiation and the outgoing radiation components at 1 km spatial resolution are used together to compute the final daily SNR dataset in a consistent manner. Validation results indicate an improvement of the mean squared error by ca. 7% with an increase in spatial detail compared to the original MSG product. The resulting pan-European ~~LST and SNR dataset~~ SNR dataset, as well as the merged LST product, can be used for hydrological modelling and as input to models dedicated to estimating evaporation and surface turbulent heat fluxes and will be regularly updated in the future.

1 Introduction

The Earth radiation budget describes how the Earth gains energy from the sun (shortwave radiation), and loses energy back
to space through its reflection and the emission of thermal (longwave) radiation (Dewitte and Clerbaux, 2017; Kato et al.,
2018). Due to the geometry of the Earth's orbit around the Sun, the yearly average net radiation at the bottom-of-atmosphere,
25 namely the Surface Net Radiation (SNR), is positive at the equator and decreases towards the poles. This geographical energy
imbalance is the main driver of the global atmospheric and oceanic circulation, which transports this energy surplus from
the equator towards the poles (Dewitte and Clerbaux, 2017; Kato et al., 2018). SNR is thus a key driver in explaining the
distribution of different climate regions and ecosystems on Earth (Köppen and Geiger, 1936), and it dominates the dynamics
of biospheric and hydrological processes (Chapin et al., 2002). For this reason, SNR is used as forcing variable in many land
30 surface models, hydrological models and satellite-based retrieval algorithms to estimate (e.g.) evaporation, runoff, soil moisture
or surface heat fluxes.

The top-of-atmosphere radiation components can be derived directly from satellites. However, dynamic atmospheric (e.g.,
cloud and aerosol optical depth) and land (e.g. emissivity, LST, albedo or biomass) properties make it more challenging to
obtain radiation estimates at the bottom-of-atmosphere, which are much more relevant to the above-mentioned biospheric and
35 hydrological processes. As it is transmitted through the atmosphere, incoming shortwave radiation is scattered and absorbed by
aerosols, gases and clouds, changing the temperature of the atmosphere and its emission of longwave radiation in all directions.
The radiation reaching the surface is partly reflected depending on land cover and surface conditions and again interacts with the
atmosphere/clouds once reflected. According to Stephens et al. (2012), on average 12% of the radiation reaching the surface is
reflected back into the atmosphere; this is known as the surface planetary albedo. Then, part of the incoming radiation absorbed
40 at the land surface is emitted towards the atmosphere as longwave radiation, as described by the Stefan–Boltzmann law. The
modelling of these atmospheric and surface processes is required to obtain SNR – i.e. the balance between shortwave and
longwave incoming and outgoing radiation at the surface – and it makes satellite-based SNR retrievals indirect and uncertain
(Kato et al., 2018).

Over the past decades, numerous satellites/instruments have been launched to enable the monitoring of the radiation budget.
45 Examples of programmes exploiting these observations to produce long-term global reliable estimates of the individual SNR
components (i.e. shortwave and longwave, and both incoming and outgoing) are the International Satellite Cloud Climatology
Project (ISCCP, Young et al. (2018)) and the Clouds and the Earth's Radiant Energy System (CERES) project (Wielicki
et al., 1996). A comparison between the CERES product and radiation estimates from global reanalyses is given by Jia et al.
(2018). Both satellite-based and reanalysis SNR products are mostly provided at a coarse (ca. $0.25°$) spatial resolution. This
50 makes them suitable for global analysis or as input in global land surface models, but insufficient for most regional-scale
studies. Nonetheless, a A few studies have already attempted to produce SNR data at higher spatial resolutions. For instance,
Verma et al. (2016) proposed a method to yield a global 5 km SNR product at 8-day resolution by combining high-resolution

variables derived from the Moderate Resolution Imaging Spectroradiometer (MODIS) Aqua satellite (including clear-sky ~~land surface temperature (LST)~~LST, emissivity, aerosol optical depth and albedo) and a radiative transfer model ~~.~~ with ancillary datasets from reanalysis. Also with a resolution of 5 km, Jiang et al. (2016, 2018) developed the GLASS daily daytime net radiation product based on Multivariate Adaptive Regression Splines, combining incoming shortwave radiation, albedo and NDVI with further meteorological ancillary variables, such as wind speed, surface pressure and air temperature. Meanwhile Jiang et al. (2023) developed a methodology, based on Landsat data and ancillary datasets, using Machine Learning to produce daily net radiation at 30 m resolution. As an alternative ~~,~~ to such methods, which are based on data from polar-orbiting satellites, to achieve a much higher temporal resolutions (sub-daily) at the expense of spatial resolution, observations from geostationary satellites can be used. The Satellite Applications Facility (LSAF) programme uses observations from the SEVIRI instrument onboard the Meteosat Second Generation (MSG) satellite to produce a SNR dataset at a spatial resolution of ca. 5–7 km (Trigo et al., 2011). These resolutions however appear still insufficient for regional water and agricultural management assessments in heterogeneous landscapes.

In this study, we present a 1 km ~~LST and SNR~~SNR, and LST, dataset for Europe using MSG and polar orbiting observations. It is based on combining operationally available hourly incoming shortwave/longwave radiation retrievals from the above-mentioned LSAF programme at moderate (5–7 km) spatial resolution with hourly LSAF LST estimates as well as higher resolution (1 km) albedo ~~observations~~ retrievals from PROBA-V and LST from Sentinel 3 (Donlon et al., 2012). The novelty of this study lies in systematically exploiting the advantages, and mitigating the disadvantages, in terms of spatial and temporal resolution of available observations, which are well validated, in a physical and consistent manner based on the surface energy balance, and assembling a net radiation dataset ~~based on~~ from the individual incoming and outgoing radiation components. This includes the development of a 1 km gap-free LST product for downscaling outgoing longwave radiation~~and the use of~~. All-sky estimates are particular important for LST as cloud cover severely restricts the availability of clear-sky retrievals and it is temporally highly variable. This is underpinned by a number of previous studies which have focused on producing all-sky LST estimates, see e.g. Xu and Cheng (2021) and Jia et al. (2023), the latter also exploiting observations from geostationary and polar-orbiting products. 1 km albedo~~for downscaled~~, for the computation of outgoing shortwave radiation, is equally calculated by combining polar and geostationary observations. The merged hourly SNR and LST data is for robustness resampled to daily time steps~~to serve as input to hydrological/land surface models or for direct analysis. The~~. The coarse-scale (5–7 km) all-sky LST estimates provided through the LSAF programme have only recently been released and the methodology here aims at exploiting these new data in an optimal manner. To our understanding, a systematic combination of these polar and geostationary retrievals with the overall goal of calculating a consistent high-resolution SNR product has not yet been undertaken. We argue that this approach based on the surface energy balance is the most consistent and, in theory, should yield the most accurate results.

The here presented published data is especially meant as a high-resolution forcing dataset for models which require SNR, such as The Global Land Evaporation Amsterdam Model (GLEAM). Such models can also benefit from high-resolution all-sky LST data making the intermediate merged LST product equally useful. In principle, the methodology can be extended to ~~other~~

~~regions where geostationary-based retrievals are available , and adapted to work with other high-resolution~~ regions where the same variables are available from other geostationary and polar-orbiting ~~satellite data.~~

satellites. The data and method are presented in detail in sections 2 and 3. All input and derived radiation components are validated against *in situ* measurements sites located across the study domain (section 4) and the SNR ~~datset~~ dataset is compared to ERA5-Land **??**(Muñoz-Sabater et al., 2021). Finally, a discussion, in respect to similar studies, and concluding remarks ~~is~~ are given in section 6. The daily SNR and LST datasets are available for scientific use under https://doi.org/10.5281/zenodo.~~7008066~~.8332222 / https://doi.org/10.5281/zenodo.~~7026612~~.8332128 as netcdf files (RNETdaily_lon_lat.nc and LSTdaily_lon_lat.nc), see **? and ?**Rains (2023b) and Rains (2023a). The spatial domain covered is -11.5 to 26.5 longitude and 35 to 71 latitude. The initial ~~datset~~ dataset is available for the years 2018–2019.

2   Data

Table 1 provides a general overview of the satellite data products used in this study. Shortwave and longwave incoming radiation components, SW_{in} and LW_{in}, as well as emissivity ε, albedo α and LST are provided by LSAF (lsa-saf.eumetsat.int) and are based on observations from the Spinning Enhanced Visible and InfraRed Imager (SEVIRI) instrument onboard the Meteosat Second Generation (MSG) geostationary satellite. These MSG products are provided with a 30-minute sampling, but to reduce data volumes we base our methodology on hourly data. The spatial resolution across the European domain is approximately 5–7 km depending on latitude. In addition, 1 km LST retrievals from the Sea and Land Surface Temperature Radiometer (SLSTR) instrument onboard Sentinel 3 as well as 1 km albedo retrievals from PROBA-V are used to compute the high-resolution LST dataset and outgoing radiation components. For the purpose of validation, we use radiation measurements from sites distributed across Europe belonging to different international networks. A more detailed description of the satellite retrievals and *in situ* data used in the study is provided in the following subsections. Note as well that ERA5-Land **??** is also used in section 4 for comparison purposes.

Variable	Satellite	Orbit	Temporal	Spatial	Coverage
SW_{in}	MSG	geostationary	hourly	5–7 km	all-sky, clear-sky+model
LW_{in}	MSG	geostationary	hourly	5–7 km	all-sky, clear-sky+model
LST	MSG	geostationary	hourly	5-7 km	all-sky, clear-sky+model
LST	Sentinel 3A	polar	2–3 days	1 km	clear-sky
ε	MSG	geostationary	daily	5–7 km	clear-sky composite
α	MSG	geostationary	daily	5–7 km	clear-sky composite
α	PROBA-V	polar	10-daily	1 km	clear-sky composite

Table 1. Overview of satellite based products used in the study with their respective temporal and spatial resolution as well as their coverage, i.e. clear-sky vs. all-sky.

2.1 Incoming shortwave/longwave radiation

We use hourly data from the LSAF programme, part of the distributed Applications Ground Segment SAF network serving as the European organisation for the Exploitation of Meteorological Satellites (EUMETSAT). The data are based on observations provided by SEVIRI onboard MSG, acquired at 12 spectral channels with 3 km resolution at nadir (1 km for the high-resolution visible channel) (Trigo et al., 2011). A detailed description of the LSAF methodology on deriving SW_{in} and its validation is given by Carrer et al. (2019a) and Carrer et al. (2019b). Details on the estimation and evaluation of LW_{in} are given by Trigo et al. (2010) and Carrer et al. (2012).

2.2 LST

The LSAF all-sky LST product based on the SEVIRI instrument onboard the geostationary Meteosat Second Generation (MSG, Martins et al. (2019)) is a combination of the clear-sky MSG level 2 product, MSLT (LSA-001), based on a Generalised Split-Window (GSW) algorithm (Trigo et al., 2008a), and output from an energy balance algorithm which is also used for the estimation of MSG 30-minute evaporation (MET-v2, LSA-311) dataset (Ghilain, 2016). The energy balance algorithm incorporates other LSAF SEVIRI-based products such as shortwave and longwave radiation fluxes, land surface albedo or vegetation, soil moisture based on the assimilation of scatterometer observations provided by the Hydrology SAF (H-SAF), and near surface meteorological information obtained from the European Centre for Medium-Range Weather Forecasts (ECMWF) operational forecasts (Ghilain et al., 2020). Within the model, each pixel is composed of different tiles representing a particular surface type based on the ECOCLIMAP-II database (Faroux et al., 2013). Pixel values are computed from the weighted average of the four most dominant tiles. The advantage of using geostationary satellites is the high temporal resolution, allowing for the characterisation of the LST diurnal cycle. An assessment of the accuracy of the LST is given by Martins et al. (2019). The

product comes with gridded uncertainty estimates, which are used in the LST merging procedure.

130   Higher-resolution, clear-sky LST estimates are obtained from Sentinel 3. The Sentinel 3 mission consists of two polar-orbiting satellites (Sentinel 3A/B) launched on February 16, 2016, and April 25, 2018 (Ghent et al., 2017; Zheng et al., 2019; Nie et al., 2021), both carrying the Sea and Land Surface Temperature Radiometer (SLSTR) instrument. They have a revisit time of 2–3 days. The instrument has nine channels, three of them covering the visible and near-infrared (VNIR) part of the spectrum, three the shortwave infrared (SWIR), and the remaining three the middle-infrared (MIR and TIR, Nie

135   et al. (2021)). For this study, we use the Climate Change Initiative (CCI) LST product provided at a spatial resolution of 0.01 degrees (https://climate.esa.int/en/odp//project/land-surface-temperature). Included in the product is the exact overpass time and as for the LSAF LST from MSG the total estimated uncertainty for each retrieval, necessary for the merging of the polar and geostationary LST data. For this initial study focusing on 2018–2019 only Sentinel 3A data was used. Sentinel 3B was launched in April 2018 and flown in tandem with Sentinel 3A from June to October of the same year after which it was moved

140   to its nominal orbit (Clerc et al., 2020). The approximate local overpass time of Sentinel 3A and Sentinel 3B thereafter is the same (ca. 10:30 am/pm) with the precise time varying and taken into account in the merging methodology (see section 3.3).

2.3   Surface emissivity

Land surface ε is required, in conjunction with LST, to calculate LW_{out}. Approaches to retrieve ε can be broadly separated into methods where LST and ε are jointly retrieved or where ε is retrieved in isolation. The latter was initially used within the LSAF

145   programme, and relied on spectral data for the various land covers based on spectral libraries, and dynamic land cover fractions (Peres and DaCamara, 2005). To overcome difficulties linked to performing the retrieval of LST and ε separately under certain conditions, e.g. in semiarid regions, LST and ε are now simultaneously retrieved by the LSAF programme including for the products we use in this study (Trigo et al., 2008b).

2.4   Albedo

150   The LSAF α product based on the MSG SEVIRI instrument is produced following three steps: (1) an atmospheric correction of top-of-atmosphere measurements to obtain reflectances, (2) a daily inversion of a semi-empirical model of the bidirectional reflectance distribution function, and then the consideration of all inversions within a temporal window to reduce the impact of outliers and reduce data gaps, and (3) the angular integration for each channel and the spectral integration (Geiger et al., 2008; Carrer et al., 2018). The product thus describes the hemispherical broadband α. As a second hemispherical broadband

155   α product, we use 1 km retrievals based on ProbaV and distributed through the Copernicus Global Land Service (CGLS). The retrieval follows the same methodology as for the LSAF α product using observations from the MSG satellite.

2.5 *In situ* measurements

For the validation of the merged hourly/daily SNR dataset and the individual radiation components we use radiation measurements taken at a total of 73 sites distributed across Europe for the 2-year study period (2018–2019). Measurements are obtained from the Baseline Surface Radiation Network (BSRN) (Driemel et al., 2018), the European Fluxes Database Cluster (http://www.europe-fluxdata.eu, EFDC), the Integrated Carbon Observation System (ICOS) (Heiskanen et al., 2021), the FLUXNET-CH4 network (Delwiche et al., 2021), and SAPFLUX (Poyatos et al., 2021). Table A, see appendix A, provides a comprehensive list of the in-sites used for this study. For a number of sites all radiation components are available (54) while for others only a subset is available. The Table includes the station ID, name, geographic coordinates and IGBP land cover class as well as which radiation components are available for validation. The following land cover classes are covered: Cropland (CRO), closed shrublands (CSH), deciduous broadleaf forest (DBF), evergreen needleleaf forest (ENF), grassland (GRA), mixed forest (MF), open shrublands (OSH), savanna (SAV), urban (URB), wetland (WET) and woody savanna (WSA).

3 Methodology

3.1 SNR calculation

SNR is computed using the radiation balance equation (1).

$$SNR = (SW_{in} + LW_{in}) - (SW_{out} + LW_{out}) \tag{1}$$

where SW_{in} is hourly incoming shortwave radiation (W m^{-2}) and LW_{in} is hourly incoming longwave radiation (W m^{-2}), both from LSAF (see section 2). SW_{out} and LW_{out} are hourly outgoing shortwave and outgoing longwave radiation (W m^{-2}), respectively, calculated as:

$$SW_{out} = SW_{in} * \alpha \tag{2}$$

$$LW_{out} = \varepsilon * \sigma * LST^4 + (1 - \varepsilon) * LW_{in} \tag{3}$$

with σ being the Stefan–Boltzmann constant (i.e. 5.67 x 10^{-8} W m^{-2} K^{-4}). Both SW_{out} and LW_{out} are to a large degree controlled by land surface properties and processes, i.e. SW_{out} by α (equation 2), and LW_{out} by ε and LST (equation 3). LST, in particular, dictates the magnitude and variability of LW_{out} over different spatial and temporal scales. Note that the term $(1 - \varepsilon) * LW_{in}$ accounts for longwave reflection (Maes and Steppe, 2012).

The focus here is on the improvement of the spatial resolution of the LSAF SW_{out} and LW_{out} by using gap-free all-sky 1 km α and LST in equations 2 and 3, respectively. The details of these datasets are given in section 3.2 and 3.3. The rationale

is based on the assumption that SW_{out} and LW_{out}, especially on the daily scale which we aggregate to, are spatially more heterogeneous than the incoming components. Therefore, by using higher-resolution α and LST, the final SNR dataset can better capture the variability induced by landscape features and conditions.

3.2 Bias correction of albedo

190 To obtain a spatially and temporally gap-free α dataset at 1 km resolution, we bias-correct the daily α from LSAF towards the retrievals from ProbaV using the mean of the temporally overlapping retrievals for 2018–2019. Remaining gaps are filled through linearly interpolating/extrapolating based on the nearest data points in the temporal domain. Prior to the bias correction, the α products are regridded using nearest-neighbour interpolation to a common $0.01°$ grid. Since both sets of α are based on the same methodology, we assume that the bias can be largely attributed to the difference in spatial resolution, but also the

195 MSG product integrating multiple observations per day, and possibly to the differences in the channels (ProbaV and SEVIRI response functions).

3.3 Merging of LST

The merging of the hourly LSAF LST (5–7 km) and Sentinel 3 LST (1 km) relies on the assumption that the diurnal cycle of LSAF is reliable in relative terms, whereas the Sentinel 3 LST can be trusted in absolute terms. This approach allows

200 us to benefit from the high temporal resolution of the geostationary data and the high spatial resolution of the Sentinel 3 observations. The all-sky LSAF product, which contains modelled LST when cloud cover prevents the direct retrieval, enables the merged gap-free LST product with Sentinel-3 resolution. After regridding the LSAF observations, using nearest-neighbour interpolation, to the $0.01°$ grid of Sentinel 3 observations, we follow a stepwise approach:

1. Temporal normalisation of Sentinel 3 daytime/nighttime observations on the hour.

205 The Sentinel 3 LST is available every ~2–3 days both during daytime (~10 am local time) and nighttime (~10 pm local time), conditioned on the presence of clear-skies. However, because of slightly differing overpass times from day to day we first normalise the Sentinel 3 daytime/nighttime observations individually to on the hour (e.g. 10:00 for daytime), using information from the diurnal cycle described by the hourly LSAF observations of the same day. For that, at each grid cell, we convert the on the hour daytime and nighttime overpass time of the Sentinel 3 observations from local time

210 to UTC. Then, when a Sentinel 3 daytime or nighttime observation is acquired, e.g. prior to that mean UTC daytime or nighttime overpass hour t, the observation is corrected through linear interpolation using the LSAF LST retrievals at t and the previous hour $t-1$ on that day:

$$Sentinel3LST_{nor} = Sentinel3LST + \Delta t * (LSAFLST_t - LSAFLST_{t-1})$$

with Δt being the difference between the on the hour mean nighttime/daytime overpass time t and the exact overpass

215 time of the specific Sentinel 3 observation on that day. We do not perform the linear interpolation if $LSAFLST_{t-1}$ and/or $LSAFLST_t$ are not clear-sky observations, i.e. the pixel is covered by cloud, and in that case, we disregard the Sentinel 3 observation. This is based on the assumption that the diurnal cycle will be less accurate when mixing clear-

sky/all-sky estimates or only relying on modelled all-sky estimates. Sentinel 3 observations with a Δt of more than 45 minutes (i.e. $\Delta t > 0.75$) are equally excluded to reduce errors from the linear interpolation.

220 2. Bias-correction of daytime/nighttime LSAF observations towards the normalised, high spatial resolution, Sentinel 3 day-time/nighttime observations.

The previously individually normalised Sentinel 3 observations $Sentinel3LST_{nor}$ are used as the basis to bias-correct the geostationary observations at the same mean on the hour overpass time t (daytime and nighttime separately) per grid cell using the means based on overlapping $Sentinel3LST_{nor}$ and $LSAFLST_t$ observations for the entire 2018–2019 225 record.

3. Bias-correction of the entire hourly geostationary $LSAFLST$ time series per grid cell by assuming that the bias cor-rected for in the previous steps applies to the subsequent hourly observations too.

We apply the bias that was applied to the geostationary daytime observations at the mean Sentinel 3 overpass time to all 230 hours of the same day after the mean Sentinel 3 overpass time and until the mean Sentinel 3 nighttime overpass time. We apply the nighttime bias correction for the hourly observations until next daytime overpass time.

4. Assimilation of the normalised Sentinel 3 observations $Sentinel3LST_{nor}$ from Step 1 into the bias-corrected hourly geostationary LSAF LST time series from Step 3.

235 At a given pixel and point in time when both $LSAFLST$ and $Sentinel3LST_{nor}$ are available, the bias-corrected geostationary LST ($LSAFLST$) is updated. This is done taking into account the uncertainty of both sets of observations using a Kalman Filter:

$$LSAFLST_a = LSAFLST + K(LSAFLST - Sentinel3LST_{nor})$$

where $LSAFLST_a$ is the updated LST at the hour t and K is the Kalman gain with the range [0, 1], computed as:

240 $$K = PH^T(HPH^T + R) - 1$$

with P being the uncertainty of the geostationary observation $LSAFLST$ and R the uncertainty of the Sentinel 3 observation at time step t. Both uncertainties are available for each individual pixel and time-step. H, the observation operator, is 1 as there is no difference between model and observation space. Normally, the update in a Kalman Filter is propagated over time through a dynamic model. Here, there is no such prognostic model to predict LST, thus we correct 245 all subsequent hourly $LSAFLST$ observations by the same amount until the next Sentinel 3 observation is available. Some ~~nore~~ more details about the LST merging and the Kalman filtering step are given in appendix F.

4 Analysis and validation

4.1 Incoming radiation fluxes

Comprehensive validation studies in literature against pyranometer measurements show the high accuracy of the LSAF radiation products; see e.g. Carrer et al. (2019b) or Lopes et al. (2022). A validation of the LSAF SW_{in} data by Roerink et al. (2012) against the CarboEurope flux tower network shows a very high accuracy, corroborated by comparing the satellite product with available radiation estimates from about 300 operational weather stations. Our own validation of both the LSAF SW_{in} and LW_{in} products shows a similar good performance, with Pearson's correlation coefficients consistently above 0.9. Figure 1 (top panels) show the correlation coefficients for all *in situ* sites in Europe for the 2018–2019 period. They are generally higher for SW_{in} than for LW_{in}. In terms of the root-mean-squared error (RMSE), SW_{in} and LW_{in} perform similarly across all sites. Few stations with a considerably worse match between observations and *in situ* data are located in Belgium for SW_{in}, and around the Alps for LW_{in}. It is fair to consider that the temporal variability of cloud cover determines to a large extent the variability of SW_{in} and LW_{in}. This is also the main information provided by satellite data (clouds and cloud optical depth via top-of-atmosphere reflectances). So the generally high R values for both SW_{in} and LW_{in} corroborate that satellite products follow reasonably well the in situ time-series. LW_{in} estimates require screen variables (LW_{in} is more indirectly linked with top-of-atmosphere observations than SW_{in}), which are derived from Numerical Weather Prediction models. Therefore it is not surprising that R and RMSE are not as good as those for SW_{in}. The accuracy of screen variables may also explain the worse performances of LW_{in} in the Alps due to the very high spatial heterogeneity. Although some orographic corrections are performed, the uncertainty is generally likely larger in mountainous regions. Since the availability of *in-situ* measurements is already fairly limited, we argue that carrying out the validation also in challenging terrain benefits the overall accuracy assessment. Figure 2 shows both SW_{in} and LW_{in} for two example sites, namely BE-Dor and IT-Lsn.
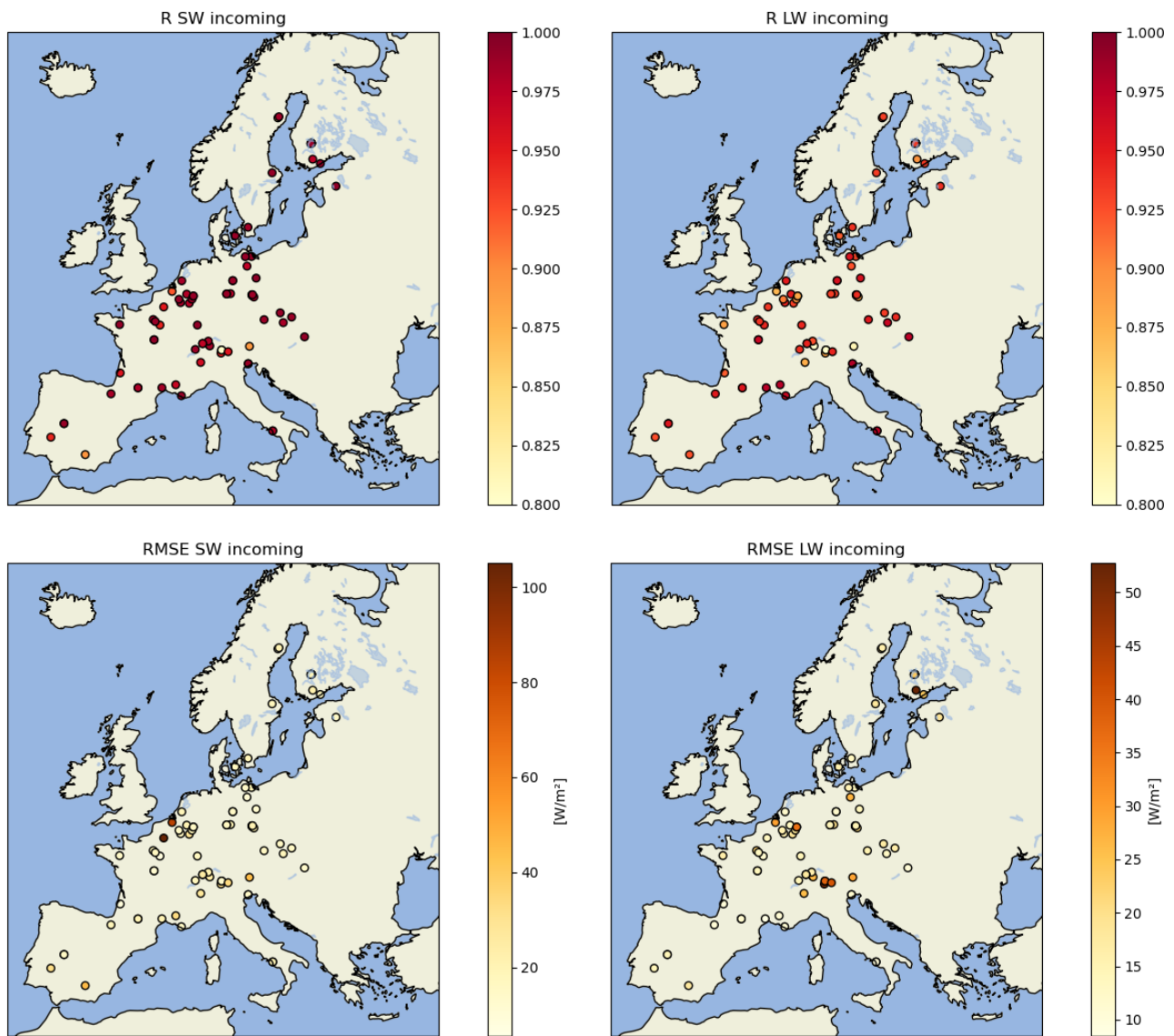
Figure 1. Validation of SW_{in} and LW_{in} from LSAF across Europe for 2018–2019 in terms of Pearson's correlation coefficient (R, top panels) and root mean squared error (RMSE, lower panels).
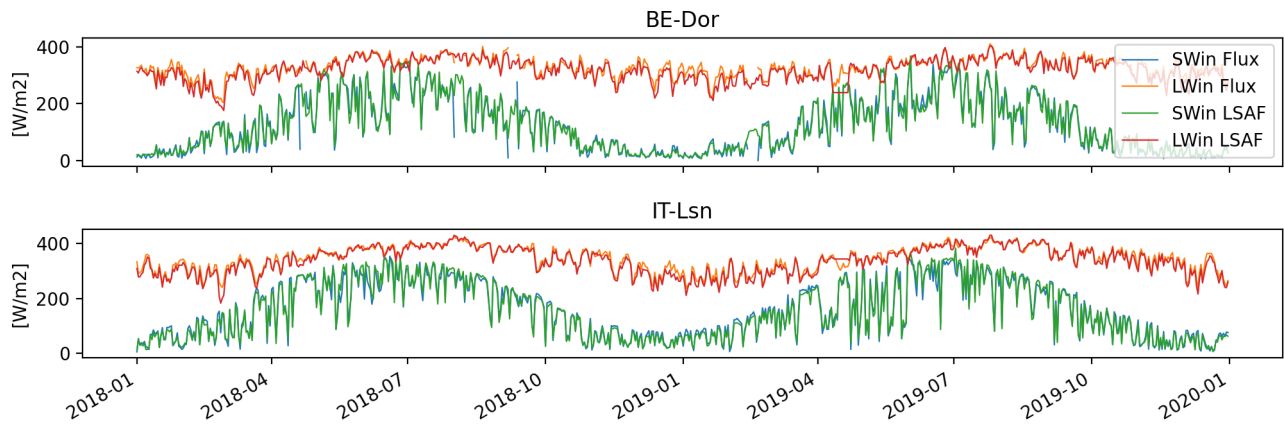
Figure 2. Daily averages of SW_{in} and LW_{in} from LSAF and ground truth for two stations BE-Dor and IT-LSN.

Additional seasonal validation statistics for the incoming radiation components are given in the appendix (see boxplots in Figures B1 and B3). In summary, for SW_{in}, R is consistently high throughout the year albeit with a higher spread of values for the individual seasons (given that the overall seasonal amplitude has a lesser impact). The Root-Mean-Squared-Error
270 (RMSE) varies slightly from season to season with the highest values in summer (April/May/June and July/August/September). This coincides with generally much higher radiation values during these months. In terms of Mean-Square-Percentage-Error (MSPE) the error is highest in the winter months. A slight bias of 5 W/m^2 is observed throughout the year although it is less pronounced during winter and spring. Validation metrics for different land cover types are also given (Figures B2 and B4) with the ESA CCI land cover product (Defourny et al., 2023) being used as its spatial resolution (300m) is more consistent with the
275 spatial resolution of the here developed data products than the land cover information provided by the FLUXNET sites. For LW_{in} (Figures B2 and B4), R again shows a higher spread for the individual seasons than for the entire study period. RMSE is highest in spring. In terms of land cover, all land cover types show high values for R whereas For RMSE, RMSPE and bias the flooded/brakish/water areas clearly show degraded performance (B4).

4.2   Land surface temperature

280 Extensive validation of the LSAF and Sentinel 3 LST products has already been performed. Both have an average accuracy below 1.5 K, although it varies across space and time. Our goal is to combine their individual strengths in terms of spatial and temporal resolution to obtain an enhanced representation of landscape heterogeneity. For an in-depth quantitative validation of the Sentinel 3 LST product we refer to Pérez-Planells et al. (2021). The LSAF LST products were validated by Trigo et al. (2008a), Göttsche et al. (2013), Göttsche et al. (2016), Martins et al. (2019) and Trigo et al. (2021). Here the validation against
285 *in situ* data is carried out not directly on LST but on LW_{out} – see section 3.3. This is based on LST validation data being limited and a validation using LW_{out} ground truth measurements thus being much more comprehensive. Furthermore, the developed LST product primarily serves the purpose of enabling a spatially downscaled LW_{out} product for the final calculation of SNR.

Figure 3 shows a comparison between the mean annual LST for 2018–2019 from LSAF and the merged LSAF/Sentinel 3
LST for two regions in Europe. The downscaled LST product shows significantly more spatial detail, especially in heteroge-
neous or topographic complex areas such as the Central System in Madrid (top row) or the Rhine Valley and its surrounding
mountainous areas (bottom row). Instead of the 2018–2019 LST average, Figure 4 shows the original LSAF LST and the
downscaled LST product for 30th June 2018. This day was chosen for no particular reason and is representative for other dates.
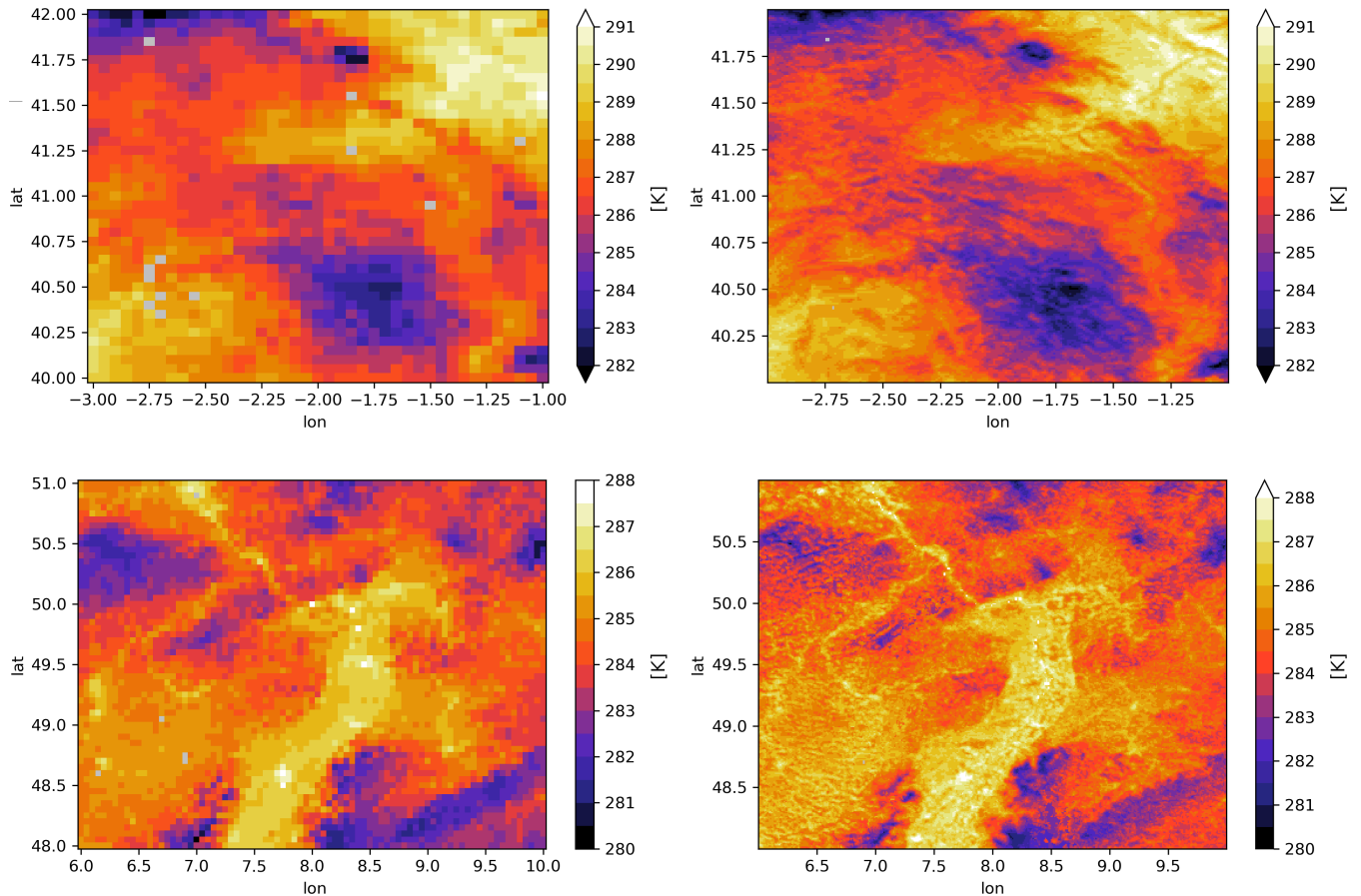
Figure 3. Mean LSAF LST (left) and merged LSAF/Sentinel 3 LST (right) for 2018–2019, showing a part of the Iberian Peninsula (top) and
the southern Rhine Valley (bottom).
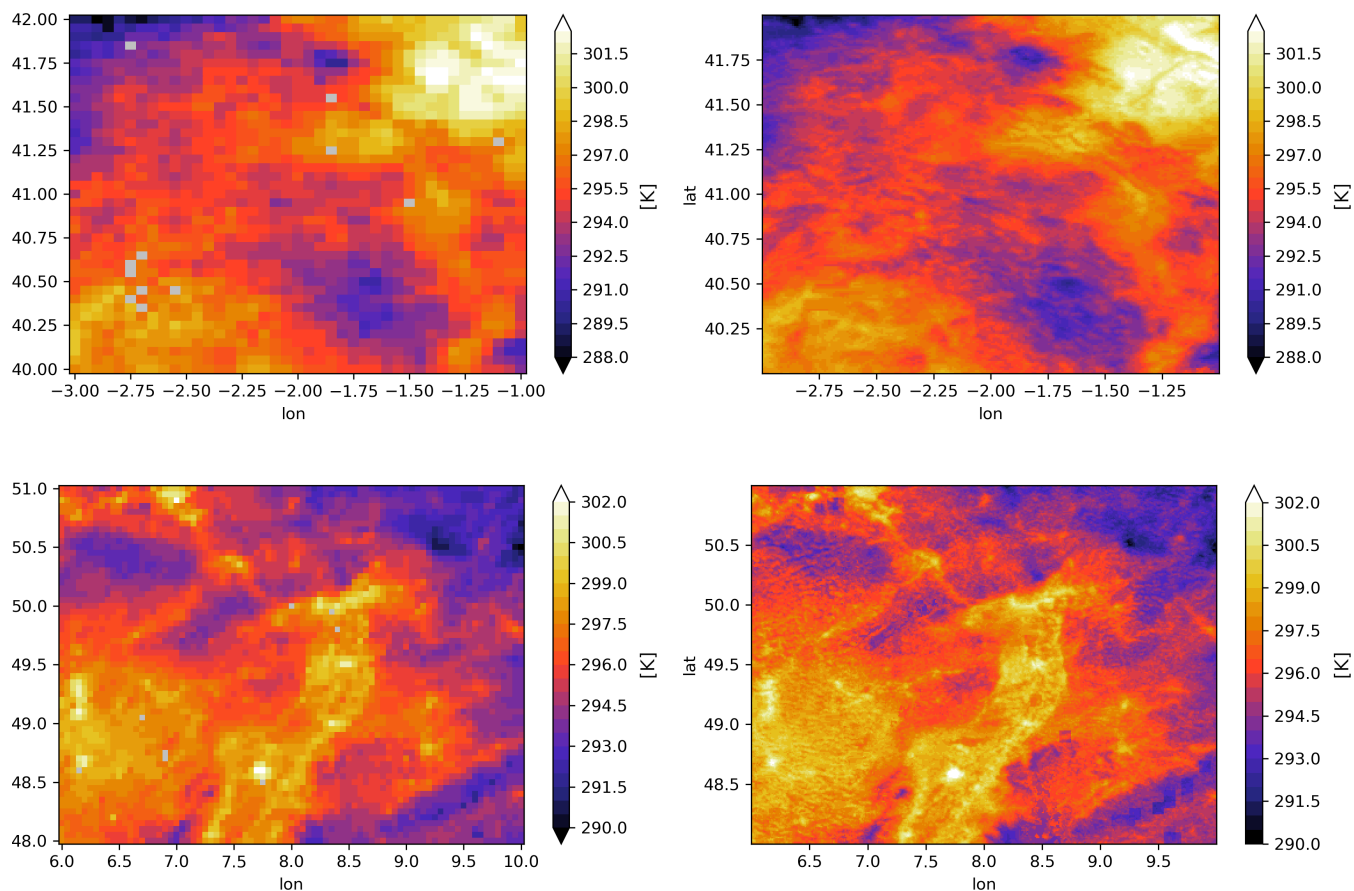
Figure 4. LSAF LST (left) and merged LSAF/Sentinel 3 LST (right) for 30th June 2018, showing the centre of the Iberian Peninsula (top) and the southern Rhine Valley (bottom).

4.3 Land surface albedo

295   Figure 5 shows the 2018–2019 mean albedo from LSAF and from the downscaled albedo product across parts of the Rhine valley, as well as the values for a single day, analogous to the LST figures 3–4. The effect of the downscaling in enhancing the spatial detail of the LSAF albedo retrievals based on PROBA-V retrievals is evident; see (e.g.) the distinct areas of low albedo surrounding the Rhine valley covered by forests and the higher albedo areas within the valley.
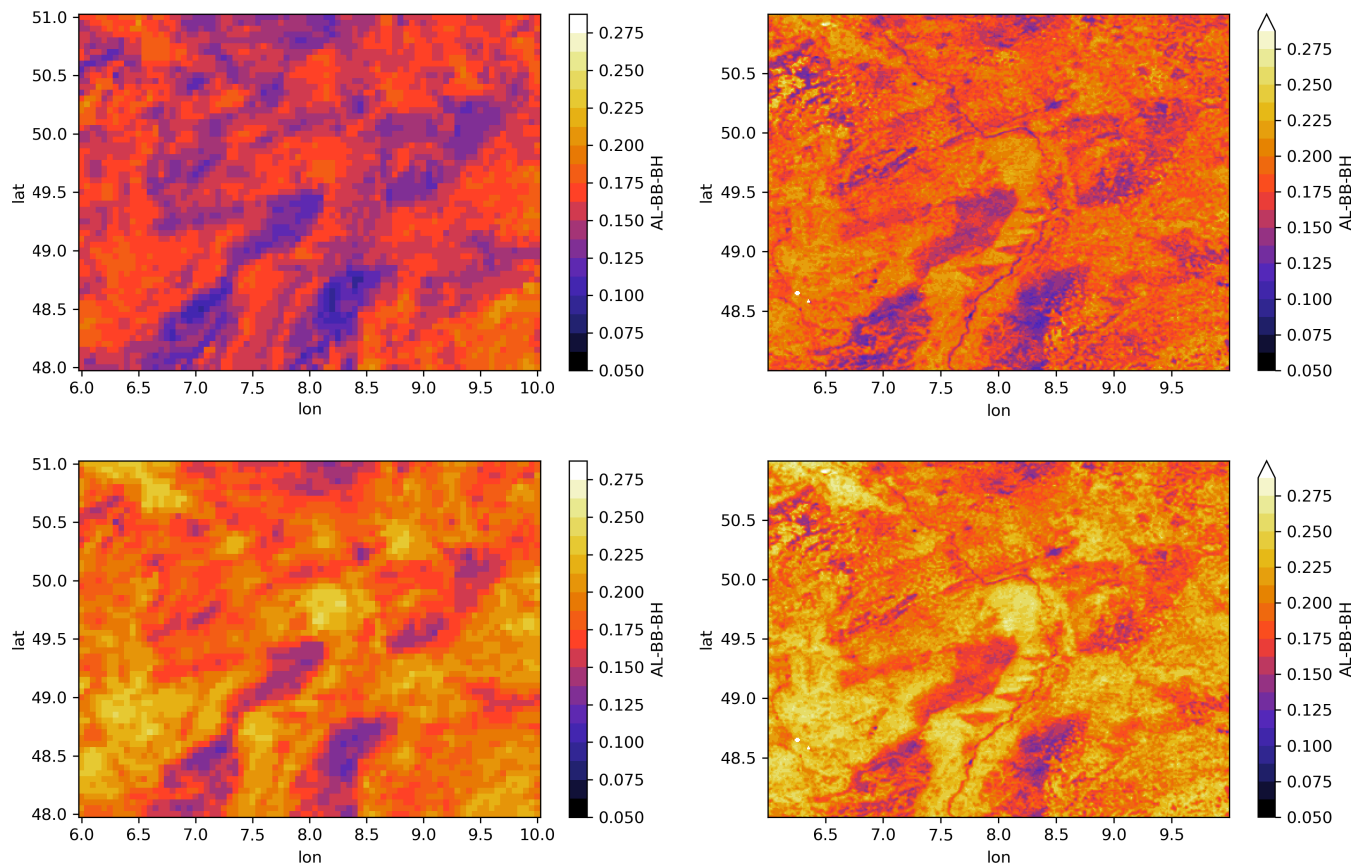
Figure 5. Mean albedo from LSAF (top left) and the downscaled dataset (top right) for 2018–2019, as well as the retrievals for the 30th June 2018 for LSAF (bottom left) and the downscaled albedo product (bottom right). The maps depict the southern Rhine valley with the river flowing from South to North through the centre of the landscape shown and then to the North-West.

4.4 Outgoing radiation fluxes

300 SW_{out} estimates, resulting from combining LSAF SW_{in} with either LSAF α or with the downscaled α dataset, are validated against *in situ* data. Likewise, LW_{out}, using either LSAF LST or the downscaled LST product, are also compared against *in situ* data. This validation therefore shows to what extent the downscaling of SW_{out} and LW_{out} in combination with emissivity data from LSAF influences the accuracy, and not only spatial detail, as shown in sections 4.2 and 4.3.

On average, both RMSE for SW_{out} and LW_{out} are lower when compared to using data from LSAF only, with a mean of
305 17.1 W/m^2 vs. 17.8 W/m^2 for SW_{out}, and 11.4 W/m^2 vs 11.04 W/m^2 for LW_{out}). Figure 6 shows the distribution of the RMSE across the available sites for the 2018–2019 period for SW_{out} and LW_{out}. The absolute values for the RMSE of LSAF as well as the difference to the downscaled products are included.
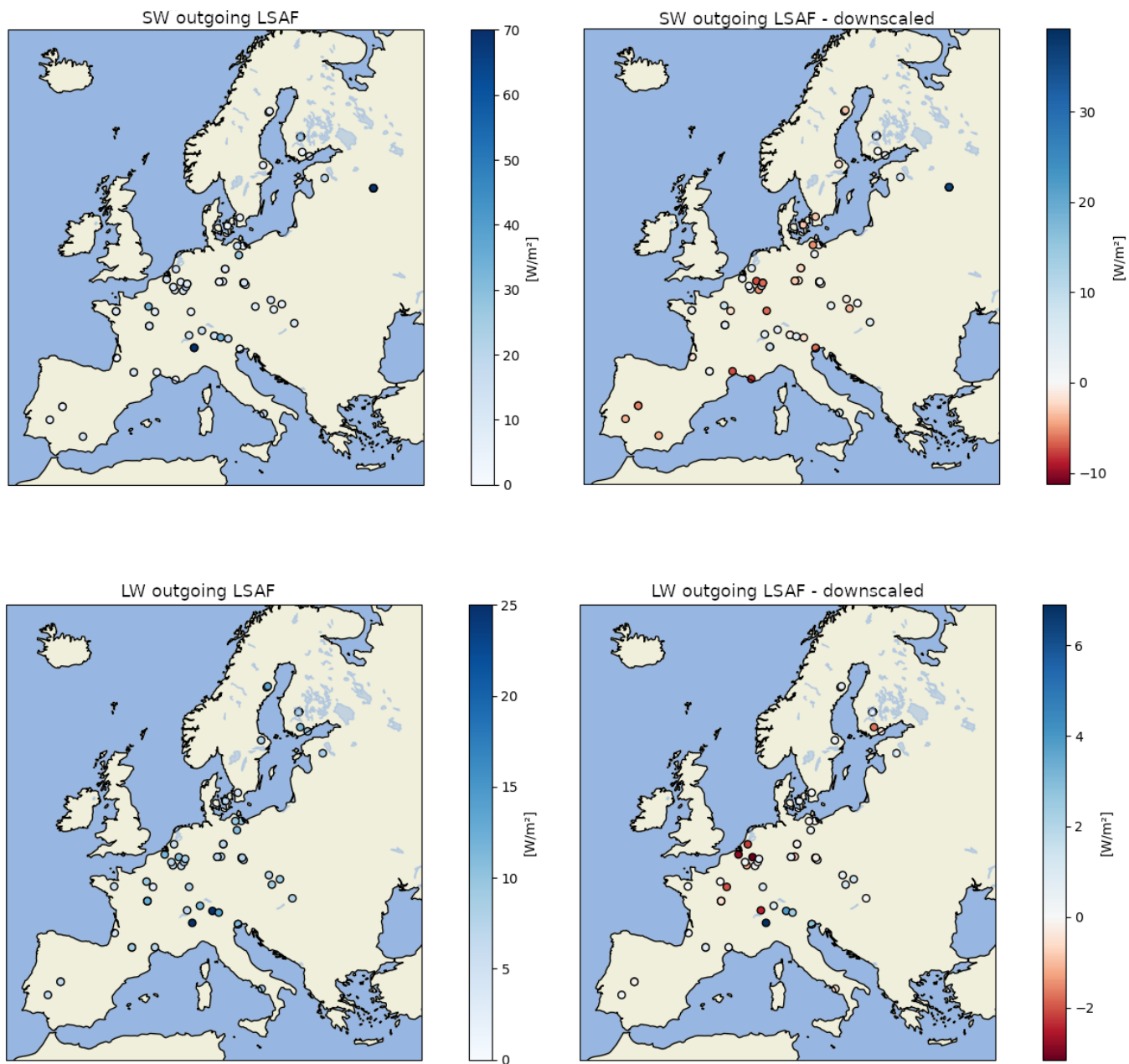
Figure 6. Validation of SW_{out} (top) and LW_{out} (bottom) in terms of RMSE. Based on LSAF only (left) and the difference to the downscaled products on the right; blue colours on the right panels indicate a better performance of the downscaled products.

Figure 7 shows R, MSE, MSPE and bias for LSAF and the downscaled product across the different CCI land cover types. For R, both SW_{out} and LW_{out} show a lower performance for the water related land cover types (see also incoming radiation validation). For MSE the same is true only for SW_{out} and here tree covered areas show a slight positive bias whereas the over

310

land cover types are on average negatively biased. For LW_{out} the bias seems less pronounced and the land cover median values are generally above or close to 0.
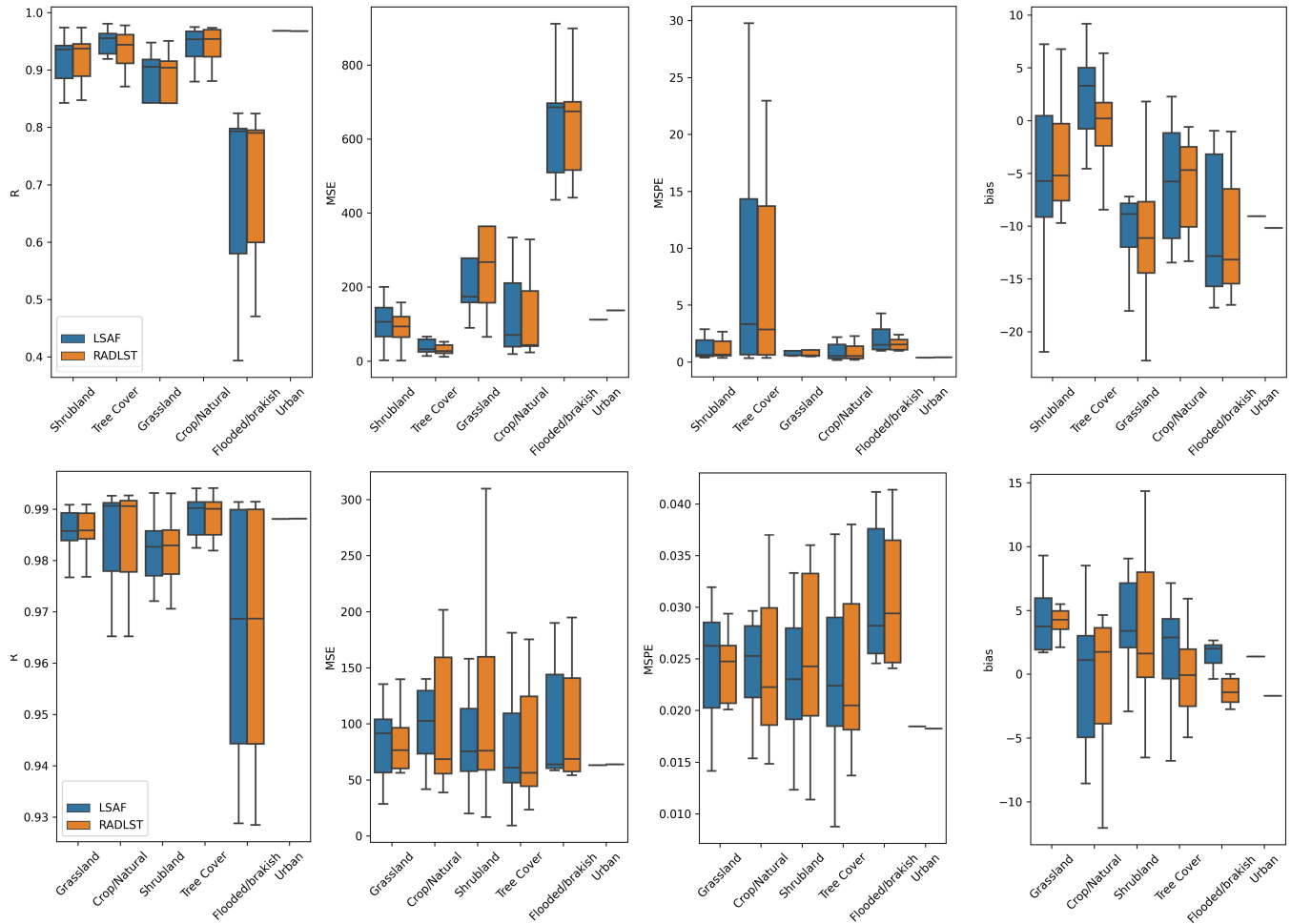
Figure 7. Validation of SW_{out} (top) and LW_{out} (bottom) radiation in terms of R, RMSE, RMSPE and bias for LSAF only and the downscaled product across different land cover types.

For a complete picture, the validation metrics are also calculated seasonally (see Figure C1 in annex). Seasonal patterns are most pronounced for RMSPE for SW_{out}, which is significantly higher during the winter months. One explanation is that
315   the calculation relies on accurate albedo values but their retrieval is especially challenging in winter due to cloud cover. Valid albedo values are linearly interpolated to fill in the data gaps and especially snow cover will have a significant impact. High errors for SW_{out} in snow cover conditions can thus be expected.

4.5 Surface net radiation

Finally, the downscaled SNR dataset, resulting from the hourly SW_{in} and LW_{in} as well as the downscaled hourly SW_{out} and LW_{out}, is validated against the available *in situ* data at daily time scales. On average, the downscaled product has a RMSE of 22.53 W/m^2 vs 23.5 W/m^2 for the MSG only product. Figure 9 shows the distribution of RMSE values across the study domain. A time series for a single example site is shown in Figure 10. We also analyse how the downscaled SNR product performs under cloudy and clear-sky conditions. Clear-sky conditions were assumed for the daily SNR product when more than 12 hours of LSAF clear-sky LST observations were available. Figure 8 shows that for clear-sky conditions both R and the bias are improved when compared to cloudy conditions. The RMSE is slightly higher for clear-sky conditions, likely linked to seasonality as clear-sky conditions are more common during summer where also the SNR values are higher.
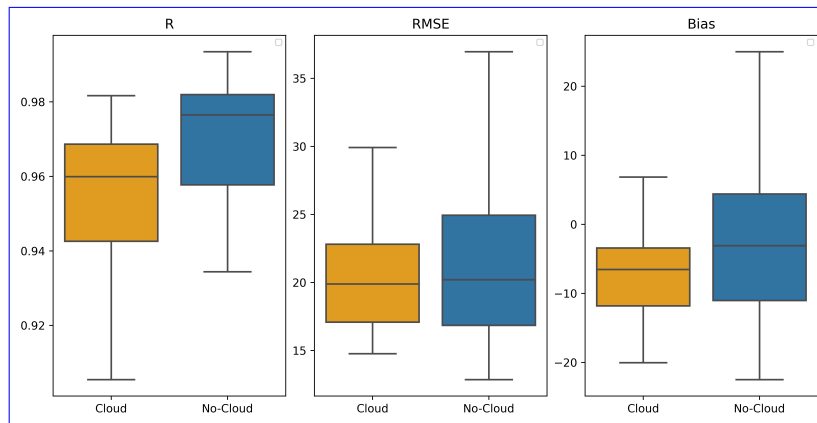
Figure 8. Validation of SNR for cloudy and clear-sky days in terms of R, RMSE and bias.

Figure 11 shows the SNR validation for the different CCI land cover types for a LSAF only based SNR as well as the downscaled product. The Figure also includes performance metrics for the ERA5-Land product ?? (Muñoz-Sabater et al., 2021) which were included to give some context. R is generally high for all products (ca. 0.95) for all sites with the exception of sites with land cover affected by water. There ERA5-Land outperforms the LSAF and downscaled SNR product in terms of R, likely due to a sub-optimal treatment of these areas in the processing of the input products. In terms of MSE ERA5-Land again outperforms the other products for water affected land cover. However, for the other land cover classes the LSAF SNR and downscaled products perform better with the downscaled dataset showing the lowest values. In terms of bias, ERA5-Land performs best with the downscaled data performing between ERA5 and the LSAF only SNR.
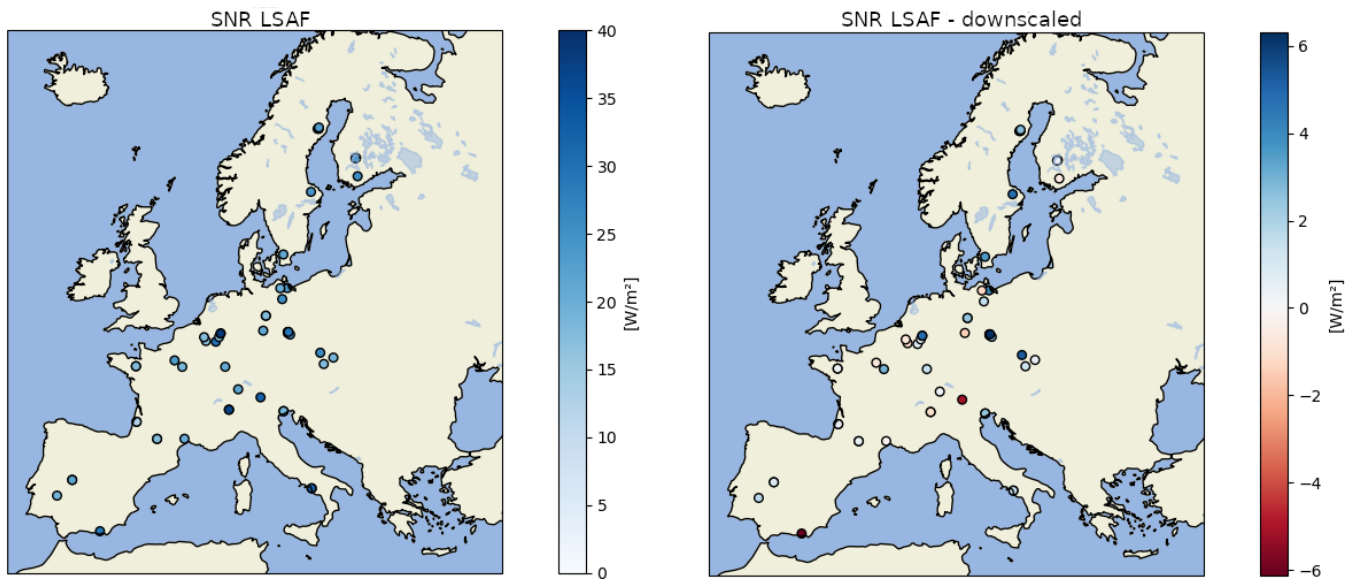
Figure 9. Validation of SNR in terms of RMSE using LSAF only (left) and the difference to the downscaled product on the right; blue colors on the right map indicate a better performance of the downscaled product.
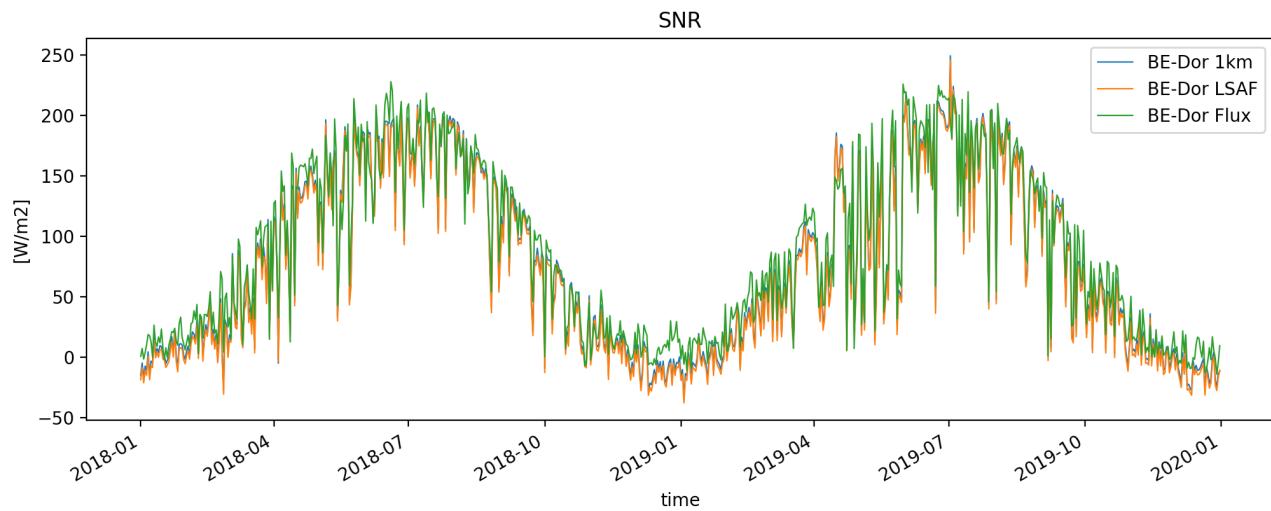
Figure 10. Daily averages of downscaled, LSAF SNR and ground truth for site IT-Lsn.
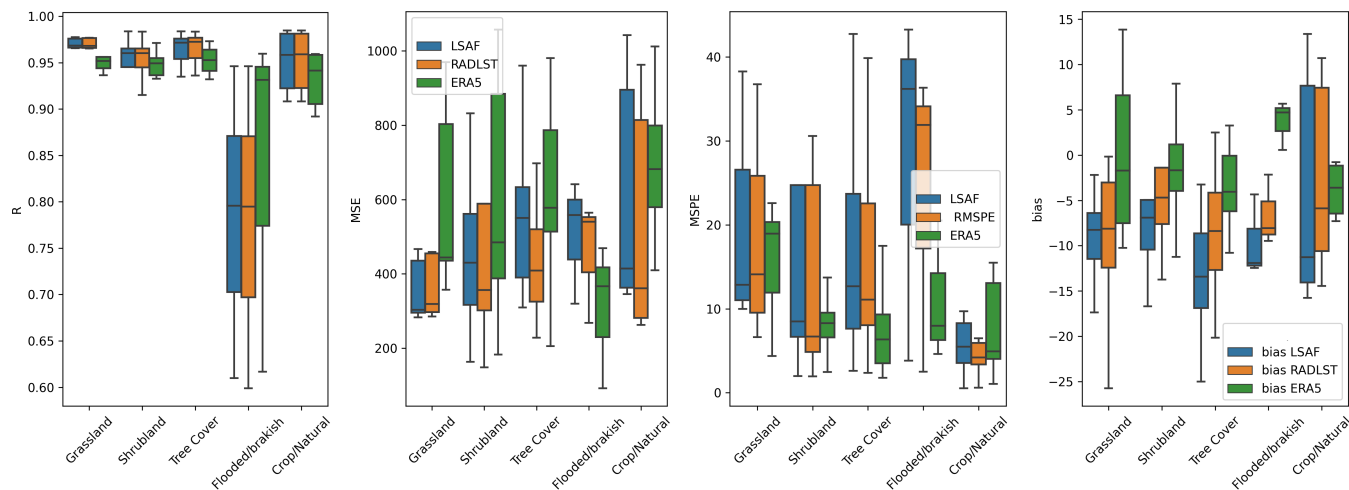
Figure 11. Validation of SNR for different CCI land cover types in terms of R, RMSE, RMSPE and bias.

For the SNR products we also carry out a seasonal analysis. The results of this are shown in Figure D1 and Figure D2 in boxplot form (see annex). Table E1 and Table E2 list all performance metrics for the entire study period as well as seasonally. For the entire 2018–2019 period, R is very similar for both datasets with R=0.93 for the downscaled product and R=0.92 for ERA5-Land. In comparison to ERA5-Land, the downscaled product has a RMSE of 22.53 vs 25.7 W^2. The average bias is lower for ERA5-Land, with -1.56 vs -6.83 W^2.

The downscaled product shows a better performance for the summer period AMJ and JAS (R=0.91 and 0.93 vs 0.83 and 0.86) and the same is true in terms of RMSE (27.58 and 22.18 W^2 vs 34.79, 29.37 W^2). The seasonal bias is lower for the downscaled product.

Figure 12 shows as an example the SNR for the downscaled product and ERA5-Land for the 30th of June over an area of western Europe. The increase in spatial resolution and therefore landscape details is clearly visible. The downscaled dataset both shows higher and lower values than ERA5-Land as it is able to resolve finer land surface features due to the high-resolution merged LST and Albedo inputs.
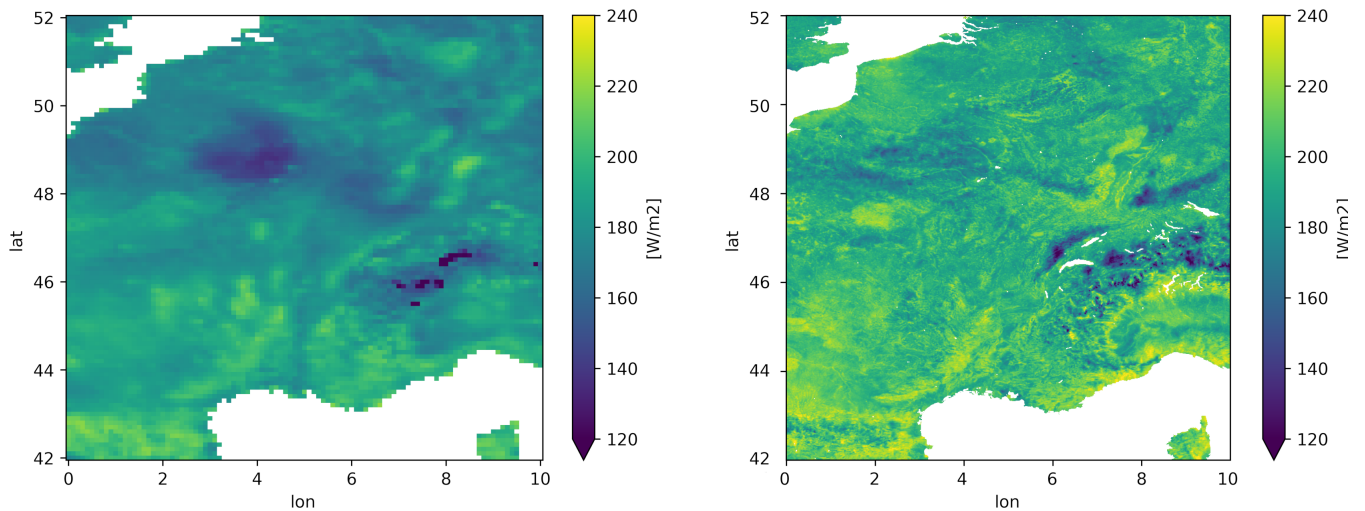
Figure 12. ~~Net radiation~~ SNR from ERA5-Land (left) and the downscaled dataset (right) for 30th June 2018. The shown maps depict a large part of western Europe covering France, Germany and Italy. ~~For the visualisation data~~ Data gaps around lakes and shorelines due to the relatively coarser resolution of the LSAF inputs have been filled through bilinear interpolation and a 1 km water mask has been applied.

~~Both surface net radiation~~

5   Discussion

350 The methodology described and validated above to produce gap-free all-sky SNR at 1 km resolution relies on producing gap-free 1 km SW_{out} and LW_{out} estimates. The methodology to produce SW_{out}, namely by means of bias-correction, is relatively straightforward. The more complex multi-stage approach taken for the all-sky LST estimates, required to compute LW_{out}, is discussed in some more detail here with regards to similar studies. Some further remarks on other available SNR products and the validation of the radiation components follow in this discussion section.

355

Examples of other gap-free LST datsets which have recently been developed are given by Shiff et al. (2021), Xu and Cheng (2021), Jia et al. (2022) or Wu et al. (2023). The approach taken by Shiff et al. (2021) was to merge clear-sky 1km MODIS LST with 0.2 degree modelled air temperature provided by the National Center for Environmental Prediction (NCEP) from the Coupled Forecast System Model version 2 (CFSv2) system. This was done by extracting the underlying seasonal behaviour from both
360 input datasets by Temporal Fourier Analysis and subsequently adding the CSFv2 anomalies to the MODIS climatology on days where no clear-sky MODIS LST observation is available. Xu and Cheng (2021) demonstrated a multi-step approach based on infrared Advanced Microwave Scanning Radiometer 2 (AMSR2) brightness temperatures, MODIS LST as well as MODIS based ancillary datasets and elevation data. First, land surface temperature ~~are~~ is retrieved from all the above datasets at 0.1 degree spatial resolution. This LST dataset is then downscaled from 0.1 degree resolution to 0.01 degree resolution by
365 using the elevation data and MODIS NDVI. Clear-sky MODIS LST data and the retrieved all-sky LST data are then bias

corrected allowing for the temporal gap-filling of the clear-sky LST retrievals. Finally, the 0.1 degree LST retrievals based on AMSR2 are assimilated into the merged 0.01 degree LST dataset by applying a multiresolution Kalman filtering approach. Jia et al. (2022) have produced all-sky diurnal, hourly LST estimates at 2 km spatial resolution based on the surface energy balance. The three step approach is based on constructing a spatiotemporal dynamic model of LST from ERA-5 in which clear-sky LST from the Advanced Baseline Imager (ABI) are assimilated. As a final step the gap-free LST record is updated by superimposing diurnal cloud effects using satellite radiation products. Wu et al. (2023) have tested an approach to produce very high-resolution, 100m gap-free LST, from a single Landsat-8 acquisition by training a Random Forest algorithm with the Landsat derived LST and ancillary variables, e.g. land cover, population density and elevation. The LST merging methodology presented in this paper shares some of the elements of the above mentioned studies, i.e. primarily the bias-correction of the coarse-scale LSAF LST observations towards Sentinel 3 (see section 3.3), as well as a Kalman Filtering approach. An in-depth validation and inter-comparison of the above mentioned products was however not the aim of this study presented here.

In terms of the calculation of the daily all-sky surface net radiation dataset, we argue that the approach taken is the most straightforward as it is based on the underlying physical principles of the individual radiation components. By relying on input products directly representing variables which are part of the surface radiation balance, any future enhancements in the source products would directly lead to improvements in future releases of the downscaled datasets. This is in contrast to studies presenting methods to produce net radiation at a similar temporal and spatial resolution which exploit statistical relationships between some well observed components, e.g. incoming radiation components from satellite, and ancillary information, e.g. land cover or NDVI, or modelled variables. Xu et al. (2022) for example train a convolutional neural network using net radiation from a selection of in-situ measurements, MERRA-2 reanalysis and AVHRR top of atmosphere (TOA) data. Jiang et al. (2023) presented two algorithms based on a Random Forest to downscale the GLASS net radiation product, either by exploiting the relationship between net radiation and shortwave radiation as well as ancillary information from ground measurements and other ancilliary datasets, or by linking net radiation to TOA observations from Landsat sensors and ancillary information. The GLASS algorithm itself is based on the Multivariate Adaptive Regression Splines (MARS) model, trained with remotely sensed incoming radiation, NDVI and albedo as well as mostly MERRA-2 meteorological variables (Jiang et al., 2016). We need to state, however, that in this paper we make no accuracy comparisons between these different approaches. Also this study indirectly relies on some ancillary variables. The retrieval of LST for instance, especially in cloudy conditions, relies on modelled processes requiring information such as vegetation phenology. In terms of validation of SNR and the individual radiation components, we also acknowledge that the FLUXNET measurements have an error (difference to the 'truth' at the local scale that they sample), but that the pixel-to-local representativeness error, i.e. the difference between the pixel truth that we aim for, and the local truth at the smaller tower footprint, is much larger. Unfortunately, we cannot solve this issue but argue that using as many stations as possible benefits the validation, also in areas where the spatial heterogeneity is very large.

6 Conclusions

400 Surface net radiation is a key input variables for many land surface and hydrological models. With increased efforts to simulate land surface processes at higher spatial resolution, the lack of high-resolution gap-free SNR ~~and LST datasets~~ is an issue. Heterogeneity of model output is then primarily driven by land surface properties for which high-resolution datasets are more frequently available (e.g. soil texture, vegetation phenology). ~~Here~~ In this paper we presented a methodology to systematically combine the advantages of frequent geostationary LST and radiation observations, enhanced with modelled data when cloud

405 cover inhibits the direct retrieval, with ~~observations~~ LST and albedo retrievals from polar-orbiting satellites at high spatial resolution. The resulting gap-free ~~all-sky LST and~~ net radiation dataset, as well as the intermediate all-sky LST dataset, for 2018–2019 across Europe uses operationally available input datasets which opens up the possibility to update the data on a close to near-real time basis. ~~While the input datasets already show a very~~ Based on the surface energy balance, and optimising each radiation component individually using input datasets with already a high accuracy, some improvements are achieved in

410 addition to a substantial increase in spatial heterogeneity and representativeness.

~~It is to be noted that while~~ While a gap-free LST datset was developed within this study, the validation of the dataset was carried out indirectly based on LW_{out} measurements. This served the purpose of the study to ultimately create a SNR dataset. ~~A number of gap-free LST datsets have been developed, see e.g. Shiff et al. (2021), Jia et al. (2022) or Wu et al. (2023), an~~

415 ~~in-depth validation and comparison of such products was however not the aim of this study. Future enhancements in the source products would directly lead to improvements in future releases of the downscaled datasets. While the developed methodology of merging two different sets of LST retrievals includes the bias correction of LSAFtowards Sentinel 3 (see section 3.3),~~ Conceptually, one of the advantages of the here developed LST merging methodology within the overall scope of producing net radiation, is its reliance on one of the LST input products being provided by LSAF, thus making the approach more

420 consistent as the incoming radiation components are also LSAF products. The use of Sentinel 3 SLSTR emissivity maps when computing the outgoing longwave radiation LW_{out} should ~~also~~ be considered in future product updates to make the methodology even more consistent. In addition, the presented results are based on the use of LST retrievals from the Sentinel 3A satellite and data from Sentinel 3B should be incorporated in ~~fthe future. For consistency~~ the future. Also, the use of Sentinel-3 based albedo instead of PROBA-V should ~~also~~ be explored.

425 A limitation in the downscaling methodology is that in the assimilation step, performed after the bias correction of LSAF LST towards Sentinel-3, there is no dynamic model to propagate the updates from the Sentinel 3 LST assimilation at the daytime or nighttime overpass time to the subsequent hours. To paliate this issue, we applied equivalent updates to the subsequent hourly LSAF observations, separately for temporal daytime/nighttime windows. Alternative approaches – such as the attenuation of the assimilation impact over time – could be explored ~~in the future~~ based on a more in-depth analysis of the diurnal

430 cycle. While the validation presented concentrated on daily aggregates, the availability of hourly LST and radiation products does make it possible to resolve the diurnal cycle, which can be a requirement for certain models.

~~The generic~~ In principle the approach developed within this study can be extended to other areas where there are both geostationary and polar-orbiting observations~~ensuring that the information they can provide is maximised~~, not necessarily the ones used for this study. The here presented dataset shall be updated in the future as we consider it to be an ideal input dataset for high-resolution land surface applications, e.g. for the Global Land Evaporation Amsterdam Model (Martens et al., 2017).

7 Data availability

The daily SNR and LST datasets for 2018–2019 are available for scientific use under https://doi.org/10.5281/zenodo.8332222 / https://doi.org/10.5281/zenodo.8332128 as netcdf files (RNETdaily_lon_lat.nc and LSTdaily_lon_lat.nc), see **?** and **?**. The spatial domain covered by the product is -11.5 to 26.5 longitude and 35 to 71 latitude.

Appendix A: In-situ sites

ID	name	lon	lat	IGBP	SW_in	LW_in	SW_out	LW_out
BE-Dor	Dorinne	4.968	50.312	GRA	x	x	x	x
BE-Lcr	Lochristi	3.850	51.112	DBF	x	x	x	x
BE-Lon	Lonzee	4.746	50.552	CRO	x	x	x	x
BE-Maa	Maasmechelen	5.632	50.980	CSH	x	x	x	x
BE-Vie	Vielsalm	5.998	50.305	MF	x	x	x	x
CH-Aws	Alp Weissenstein	9.790	46.583	GRA	x	x		
CH-Cha	Chamau	8.410	47.210	GRA	x	x	x	x
CH-Dav	Davos	9.856	46.815	ENF	x	x	x	x
CH-Fru	Früebüel	8.538	47.116	GRA	x	x		
CH-Lae	Laegern	8.364	47.478	MF	x	x		
CH-Oe2	Oensingen	7.734	47.286	CRO	x	x		
CZ-Lnz	Lanzhot	16.946	48.682	MF	x	x	x	x
CZ-RAJ	Rajec	16.697	49.444	ENF	x	x	x	x
CZ-Stn	Stitna	17.970	49.036	DBF	x	x	x	x
CZ-Wet	Trebon	14.770	49.025	WET	x	x	x	x
DE-Akm	Anklam	13.683	53.866	WET	x	x	x	x
DE-Dgw	Dagowsee	13.054	53.151	WET	x	x	x	x
DE-Geb	Gebesee	10.915	51.100	CRO	x	x	x	x
DE-Gri	Grillenburg	13.513	50.950	GRA	x	x	x	x
DE-Hai	Hainich	10.452	51.079	DBF	x	x	x	x
DE-HoH	Hohes Holz	11.219	52.085	DBF	x	x	x	x
DE-Hte	Huetelmoor	12.176	54.210	WET	x			
DE-Hzd	Hetzdorf	13.490	50.964	DBF	x	x	x	x

DE-Kli	Klingenberg	13.522	50.893	CRO	x	x	x	x
DE-Obe	Oberbärenburg	13.721	50.787	ENF	x	x	x	x
DE-RuR	Rollesbroich	6.304	50.622	GRA	x	x	x	x
DE-RuS	Selhausen Juelich	6.447	50.866	CRO	x	x	x	x
DE-Tha	Tharandt	13.565	50.963	ENF	x	x	x	x
DE-Zrk	Zarnekow	12.889	53.876	WET	x	x	x	x
DK-Sor	Soroe	11.645	55.486	DBF	x	x	x	x
ES-Abr	Albuera	-6.786	38.702	SAV	x	x	x	x
ES-Cnd	Conde	-3.228	37.915	WSA	x	x	x	x
ES-LM1	Majadas del Tietar North	-5.779	39.943	SAV	x	x	x	x
ES-LM2	Majadas del Tietar South	-5.776	39.935	SAV	x	x	x	x
FI-Hyy	Hyytiala	24.295	61.847	ENF	x	x	x	x
FI-Kmp	Kumpula	24.961	60.203	URB	x	x	x	x
FI-Kvr	Kuivajarvi	24.280	61.847	WAT	x	x	x	x
FI-Let	Lettosuo	23.960	60.642	ENF	x	x	x	x
FI-Sii	Siikaneva	24.193	61.833	WET	x	x	x	x
FI-Var	Varrio	29.610	67.755	ENF	x			
FR-Aur	Aurade	1.106	43.550	CRO	x	x	x	x
FR-Bil	Bilos	-0.956	44.494	ENF	x	x	x	x
FR-EM2	Estrees-Mons A28	3.021	49.872	CRO	x	x		
FR-FBn	Font-Blanche	5.679	43.241	MF	x	x	x	x
FR-Fon	Fontainebleau	2.780	48.476	DBF	x	x	x	x
FR-Gri	Grignon	1.952	48.844	CRO	x	x	x	x
FR-Hes	Hesse	7.065	48.674	DBF	x	x	x	x
FR-LGt	La Guette	2.284	47.323	WET	x	x	x	x
FR-Mej	Mejusseaume	-1.796	48.118	GRA	x	x	x	x
FR-Pue	Puechabon	3.596	43.741	EBF	x	x	x	x
IT-BCi	Borgo Cioffi	14.957	40.524	CRO	x	x	x	x
IT-Cp2	Castelporziano2	12.357	41.704	EBF	x	x		x
IT-Lsn	Lison	12.750	45.740	OSH	x	x	x	x
IT-MtM	Muntatschinig Meadow	10.580	46.687	GRA	x	x	x	x
IT-Ren	Renon	11.434	46.587	ENF	x		x	
IT-SR2	San Rossore 2	10.291	43.732	ENF	x	x	x	x
IT-Tor	Torgnon	7.578	45.844	GRA	x	x	x	x
RU-Fy2	Fyodorovskoye	32.902	56.448	ENF	x	x	x	x
RU-Fyo	Fyodorovskoye	32.922	56.462	ENF	x	x	x	x
SE-Deg	Degero	19.557	64.182	WET	x	x	x	x
SE-Htm	Hyltemossa	13.419	56.098	ENF	x	x	x	x

SE-Lnn	Lanna	13.102	58.341	CRO	x			
SE-Nor	Norunda	17.480	60.086	ENF	x	x	x	x
SE-Svb	Svartberget	19.775	64.256	ENF	x	x	x	x
bud	Budapest-Lorinc	19.182	47.429		x	x	x	x
cab	Cabauw	4.927	51.971		x	x	x	x
car	Carpentras	5.030	44.050		x	x		
cnr	Cener	-1.601	42.816		x	x		
lin	Lindenberg	14.122	52.210		x	x		
pal	Palaiseau	2.208	48.713		x	x		
pay	Payerne	6.944	46.815		x	x	x	x
son	Sonnblick	12.958	47.054		x	x		
tor	Toravere	26.462	58.264		x	x	x	x

Appendix B: Incoming radiation fluxes
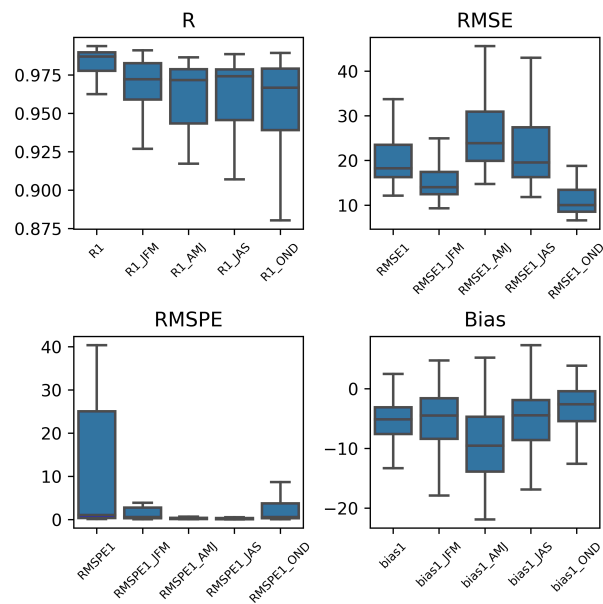
Figure B1. Validation of LSAF SW_{IN} in terms of R, RMSE, RMSPE and bias for the entire period as well as seasonally.
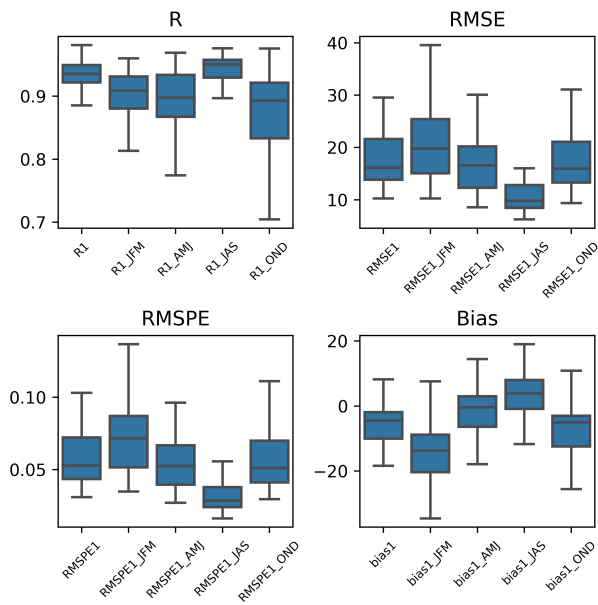
Figure B2. Validation of LSAF LW_{in} in terms of R, MSE, MSPE and bias for the entire period as well as seasonally.
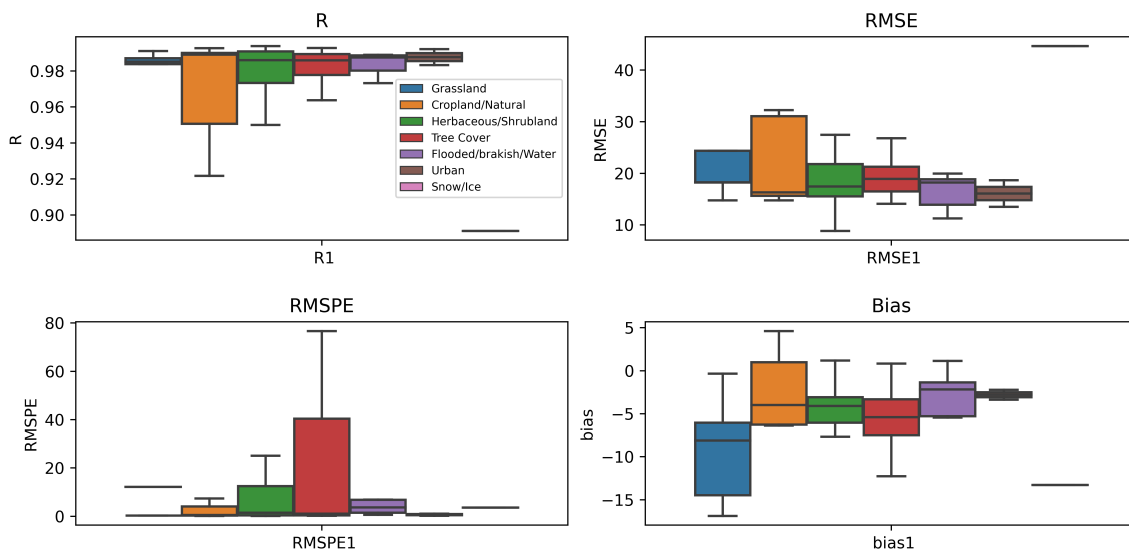
Figure B3. Validation of LSAF SW_{in} in terms of R, RMSE, RMSPE and bias for different land cover types.
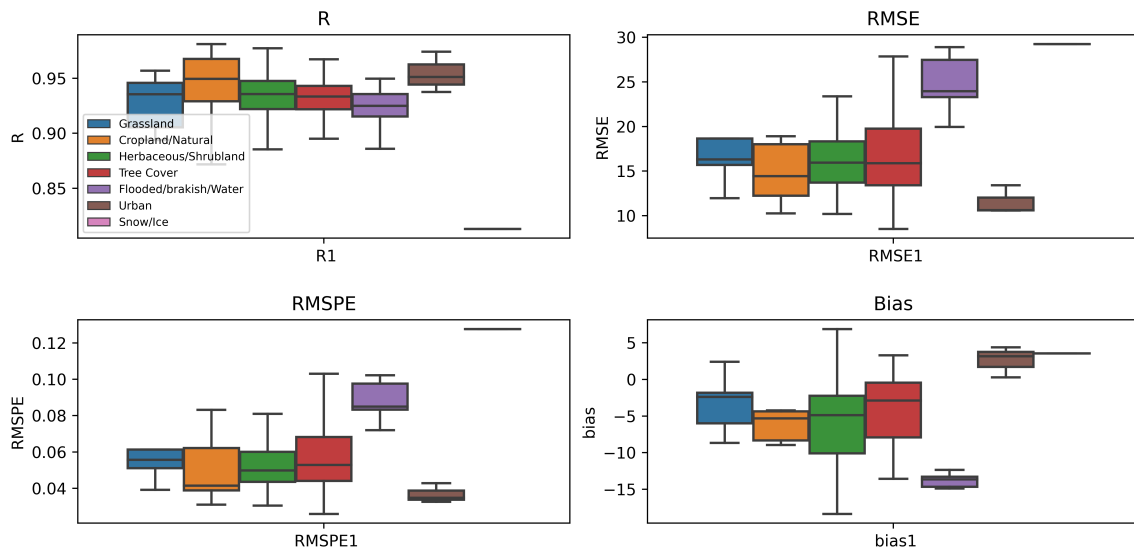
Figure B4. Validation of LSAF LW_{in} in terms of R, MSE, MSEP and bias for different land cover types.

Appendix C: Outgoing radiation fluxes
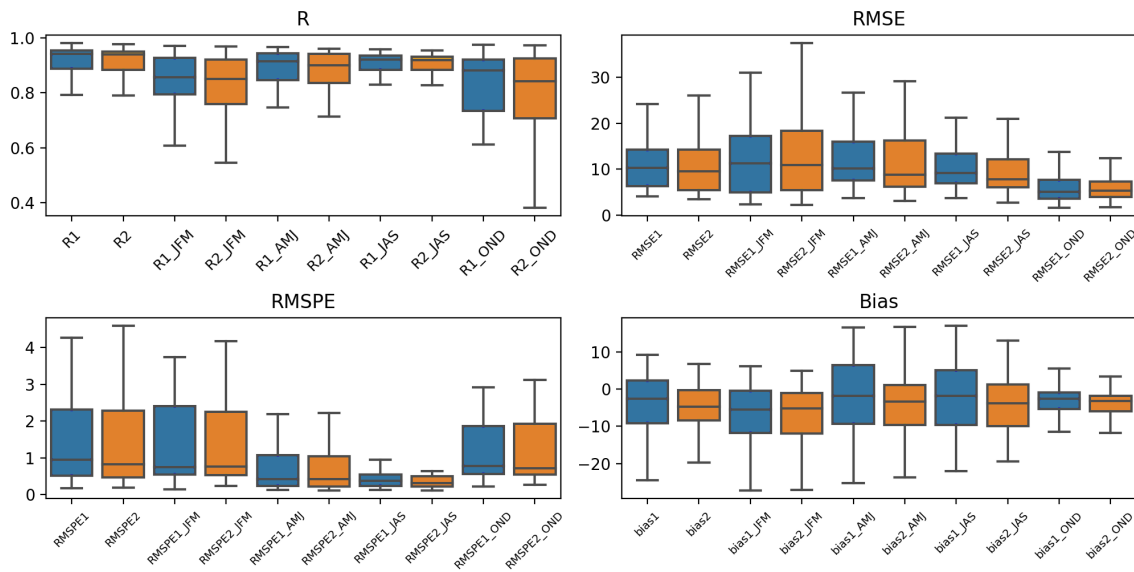
Figure C1. Validation of SW_{OUT} in terms of R, RMSE, RMSPE and bias using LSAF only (R1) and the ~~the~~ downscaled product (R2) for the entire period as well as seasonally.
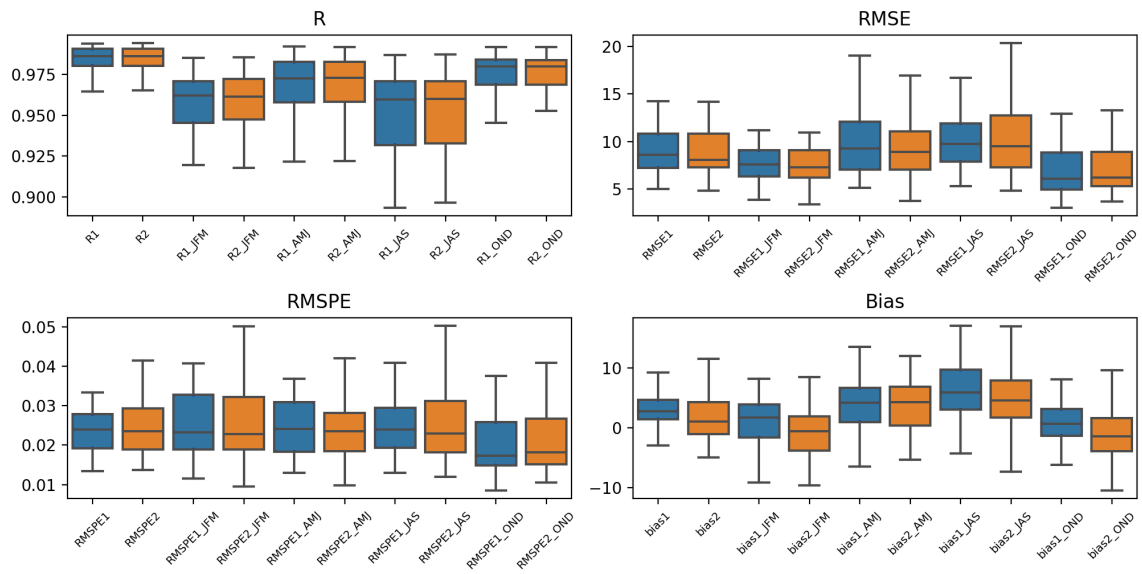
Figure C2. Validation of LW_{out} in terms of R, MSE, MSPE and bias using LSAF only (R1) and the the downscaled product (R2) for the entire period as well as seasonally.

Appendix D: Net radiation
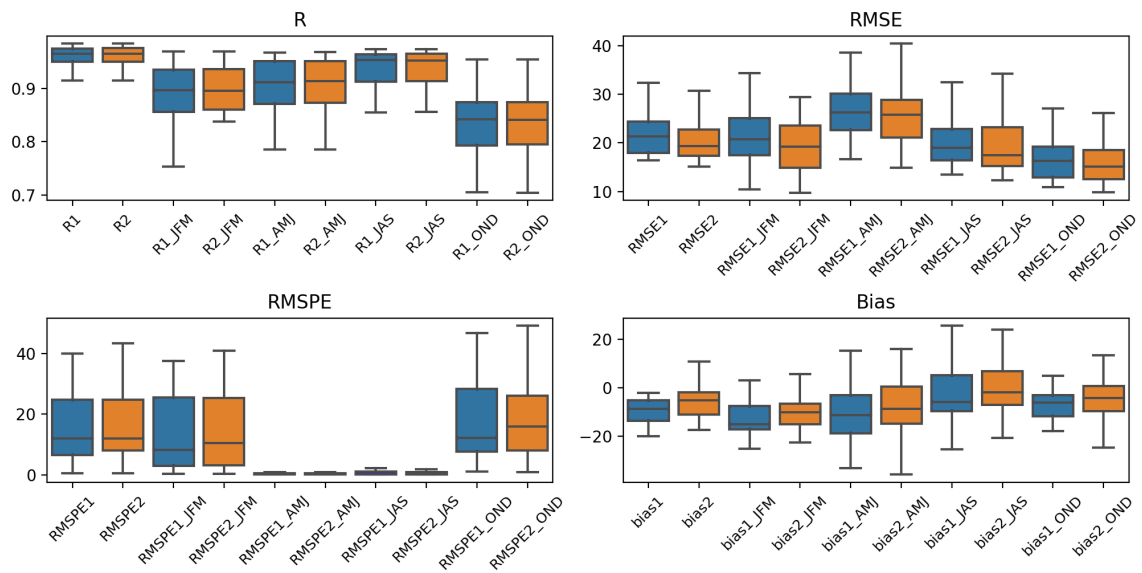
Figure D1. Validation of SNR in terms of R, RMSE, RMSPE and bias using LSAF only (R1) and the downscaled product (R2) for the entire period as well as seasonally.
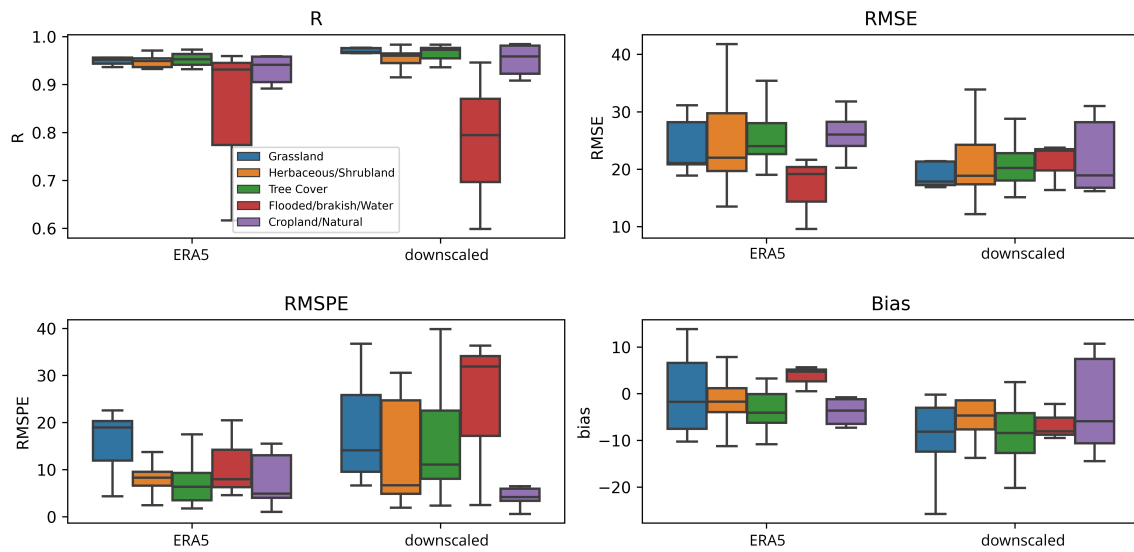
Figure D2. Validation of ERA5-Land and downscaled net radiation product against in-situ measurements in terms of R, RMSE, RMSEP and bias for different land cover types.

445 **Appendix E: Overall validation statistics**

	R	MSE	MSPE	bias
$SWin$	0.97	876	7.59	-7.65
$LWin$	0.93	420	0.06	-6.99
$SWout$ LSAF	0.87	317	7.99	-4.55
$SWout$ RADLST	0.87	293	6.93	-5.5
$LWout$ LSAF	0.97	132	0.029	2.36
$LWout$ RADLST	0.97	122	0.028	0.81
RNET LSAF	0.93	551	17	-9.06
RNET RADLST	0.93	515	15.89	-6.11
ERA5	0.93	654	10.04	-1.89

Table E1. Performance metrics for radiation components for the 2018–2019 study period.

	R Q1	MSE Q1	MSPE Q1	bias Q1	R Q2	MSE Q2	MSPE Q2	bias Q2	R Q3	MSE Q3	MSPE Q3	bias Q3	R Q4	MSE Q4	MSPE Q4	bias Q4
$SWin$	0.96	535	6.66	-6.88	0.95	1320	1.09	-12.2	0.94	1431	1.91	-8.02	0.95	399	5.97	-4.92
$LWin$	0.89	598	0.08	-15	0.88	361	0.05	-2.39	0.93	228	0.03	1.05	0.87	433	0.06	-9.29
$SWout$ LSAF	0.84	588	11.5	-9.14	0.87	490	1.99	-3.26	0.89	148	4.63	-2.72	0.8	129	3.36	-4.01
$SWout$ RADLST	0.82	562	9.25	-9.66	0.87	441	1.66	-5.07	0.89	121	3.87	-4.23	0.78	124	3.22	-4.32
$LWout$ LSAF	0.92	114	0.029	0.87	0.94	170	0.03	4.31	0.92	145	0.02	5.94	0.95	96	0.02	0.27
$LWout$ RADLST	0.93	101	0.028	-0.83	0.95	163	0.03	2.87	0.93	134	0.02	4.6	0.96	90	0.02	-1.36
RNET LSAF	0.84	527	21	-11.87	0.91	860	1.11	-10.55	0.93	503	1.96	-4.17	0.77	336	22.24	-7.82
RNET RADLST	0.84	481	20	-9.39	0.91	800	1.14	-6.6	0.93	477	2.03	-0.76	0.8	316	19.79	-5.51
ERA5	0.84	407	10.49	47	0.83	1187	1.07	-61	0.86	844	2.43	-50	0.82	274	13.86	53.46

Table E2. Seasonal performance metrics for radiation components.

Appendix F: Downscaling of LSAF LST with Sentinel 3 LST

For the downscaling/merging of the LSAF with Sentinel 3 based LST retrievals described in section 3.3 some more detail is given here. Figure F1 shows as an example the mean Sentinel 3 LST and its bias towards LSAF observations for daytime (10am. local time) observations. Across the domain the bias is neither systematically negative nor positive, highlighting the generally high agreement between LSAF and Sentinel 3 observations, and it is more linked to geographic features. The UTC time of the underlying Sentinel 3 data is different for each pixel/day across the domain and the LSAF data the bias is calculated against is thus a composite from different acquisition times. The Sentinel 3 observations are normalised to the one the hour Sentinel 3 mean overpass time per pixel to enable a more correct match-up between Sentinel 3 and LSAF (as the LSAF data is representative for on the hour). This is done through linear interpolation using the LSAF LST difference between the full hour before and after the exact overpass time of each Sentinel 3 observation. The bias correction is then performed between LSAF LST and the normalised Sentinel 3 observations for each pixel individually for the entire study period. A seasonal bias correction should be considered in the future.
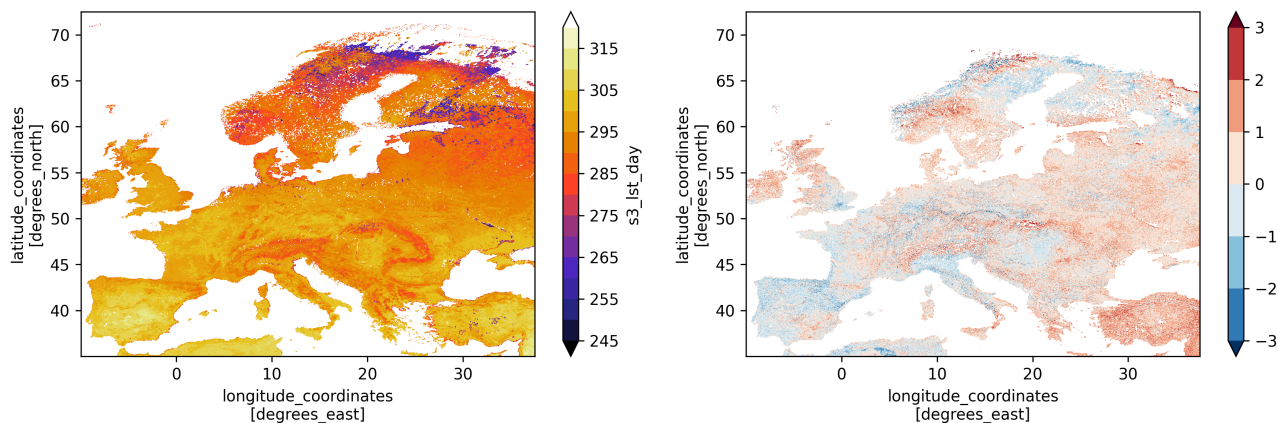
Figure F1. Mean LST of Sentinel 3 daytime (ca. 10am) observations (left) and bias towards LSAF observations (right).

After the full bias correction of the hourly LSAF data the normalised Sentinel 3 observations are assimilated into this time series for each pixel. The respective uncertainties of both Sentinel 3 and LSAF LST retrievals for each pixel/timestep are therefore taken into account. Figure F2 shows as an example for a single day the assimilation diagnostics. The top row shows the the Sentinel 3 LST retrieval (left), the uncertainty map of the Sentinel 3 observation (middle) and the uncertainty of the LSAF observations (right). The Kalman Gain (bottom left) is based on the two uncertainties and a value of 1 would fully trust the Sentinel 3 observation, whereas 0 would result in no assimilation update. The difference, i.e. innovation, between the Sentinel 3 observation and LSAF LST, is shown in the lower middle. The increment, the actual update, is the innovation multiplied by the Kalman Gain and is shown in the bottom right.
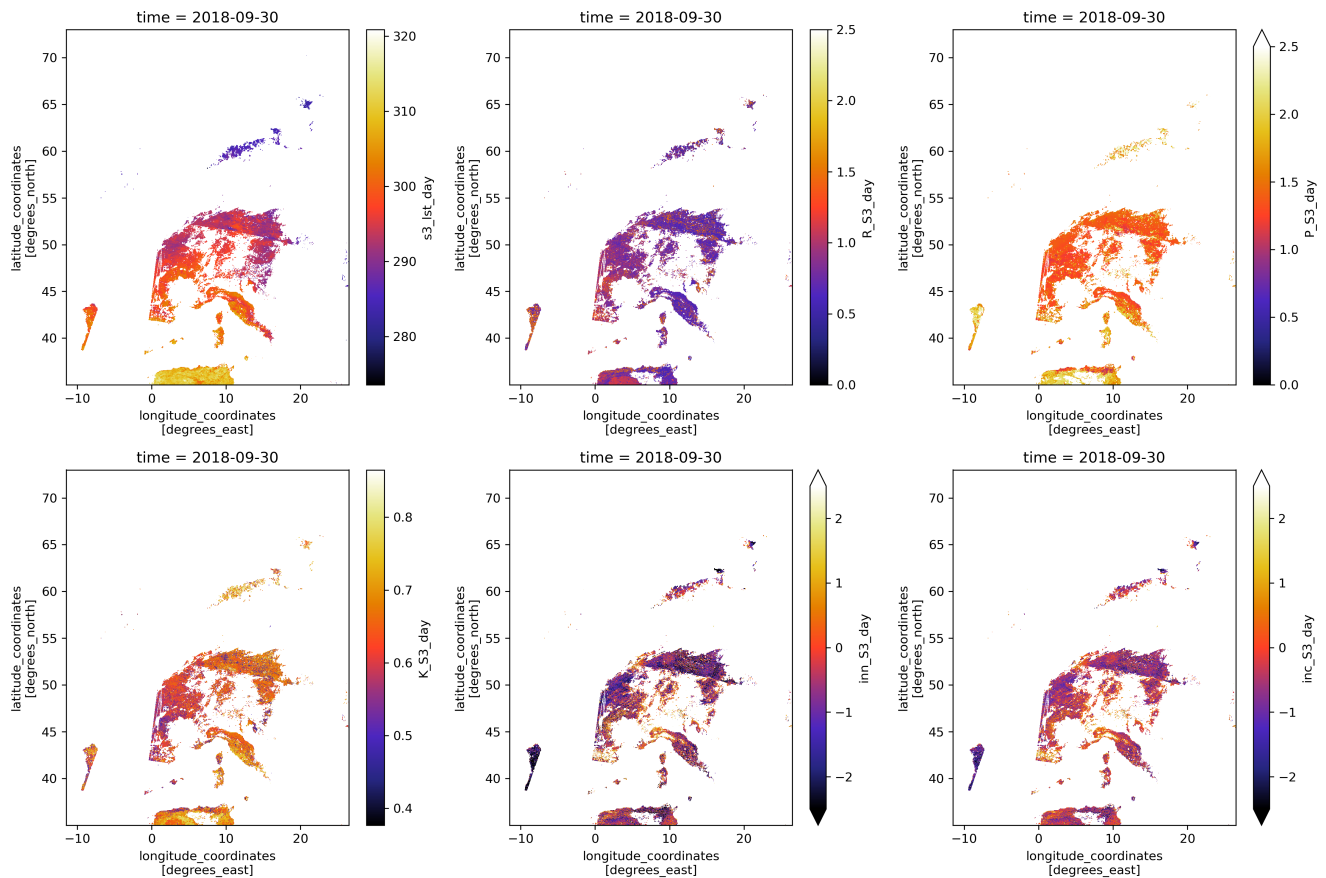
Figure F2. Sentinel 3 LST retrievals (top left), uncertainty of Sentinel 3 LST retrievals (top middle), uncertainty of LSAF LST retrievals (top right) and Kalman Gain (bottom left), innovations (bottom middle), increments (bottom right).

Figure F3 shows the 2018–2019 mean assimilation diagnostics for the daytime Sentinel 3 assimilation. The innovation (left) is fairly close to zero showing that the bias correction results in the Sentinel 3 observations being on average spread evenly around the bias corrected LSAF time series as intended. The mean increment (middle), the actual correction applied to the

470 LSAF estimates, shows similar spatial patterns. The mean Kalman Gain is shown on the right.
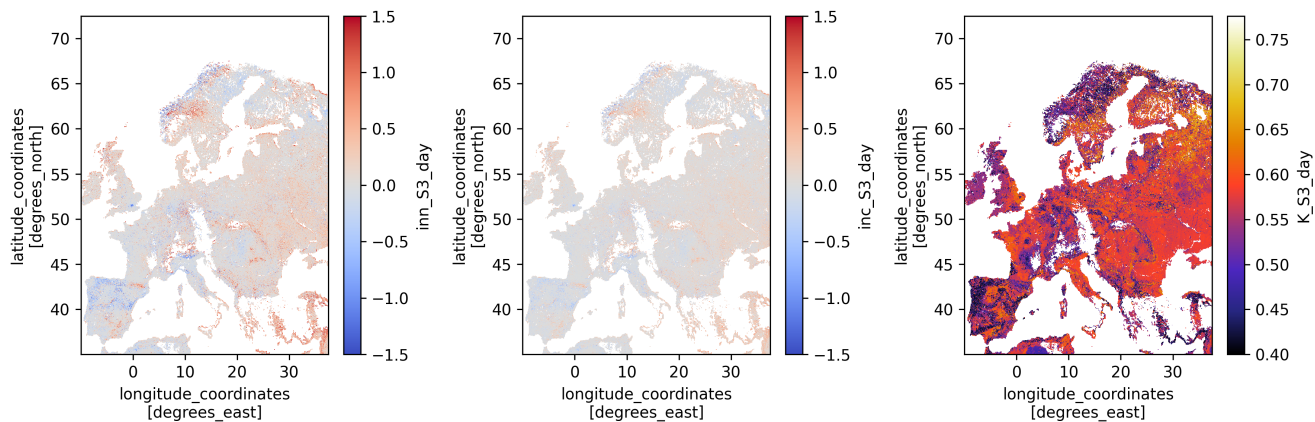
Figure F3. Mean Innovation (left), increments (middle) and Kalman Gain (right) for daytime Sentinel 3 LST assimilation.

Competing interests. No competing interests are present.

References

Carrer, D., Lafont, S., Roujean, J.-L., Calvet, J.-C., Meurey, C., Le Moigne, P., and Trigo, I.: Incoming solar and infrared radiation derived
475   from METEOSAT: Impact on the modeled land water and energy budget over France, Journal of Hydrometeorology, 13, 504–520, 2012.

Carrer, D., Moparthy, S., Lellouch, G., Ceamanos, X., Pinault, F., Freitas, S. C., and Trigo, I. F.: Land surface albedo derived on a ten daily
basis from Meteosat Second Generation Observations: The NRT and climate data record collections from the EUMETSAT LSA SAF,
Remote Sensing, 10, 1262, 2018.

Carrer, D., Ceamanos, X., Moparthy, S., Vincent, C., C. Freitas, S., and Trigo, I. F.: Satellite Retrieval of Downwelling Shortwave Surface
480   Flux and Diffuse Fraction under All Sky Conditions in the Framework of the LSA SAF Program (Part 1: Methodology), Remote Sensing,
11, https://doi.org/10.3390/rs11212532, 2019a.

Carrer, D., Moparthy, S., Vincent, C., Ceamanos, X., C. Freitas, S., and Trigo, I. F.: Satellite Retrieval of Downwelling Shortwave Surface
Flux and Diffuse Fraction under All Sky Conditions in the Framework of the LSA SAF Program (Part 2: Evaluation), Remote Sensing,
11, https://doi.org/10.3390/rs11222630, 2019b.

485 Chapin, F. S., Matson, P. A., Mooney, H. A., and Vitousek, P. M.: Principles of terrestrial ecosystem ecology, 2002.

Clerc, S., Donlon, C., Borde, F., Lamquin, N., Hunt, S. E., Smith, D., McMillan, M., Mittaz, J., Woolliams, E., Hammond, M., Banks, C.,
Moreau, T., Picard, B., Raynal, M., Rieu, P., and Guérou, A.: Benefits and Lessons Learned from the Sentinel-3 Tandem Phase, Remote
Sensing, 12, https://doi.org/10.3390/rs12172668, 2020.

Defourny, P., Lamarche, C., Brockmann, C., Boettcher, M., Bontemps, S., De Maet, T., Duveiller, G., Harper, K., Hartley, A., Kirches, G.,
490   et al.: Observed annual global land-use change from 1992 to 2020 three times more dynamic than reported by inventory-based statistics,
2023.

Delwiche, K. B., Knox, S. H., Malhotra, A., Fluet-Chouinard, E., McNicol, G., Feron, S., Ouyang, Z., Papale, D., Trotta, C., Canfora, E.,
et al.: FLUXNET-CH 4: a global, multi-ecosystem dataset and analysis of methane seasonality from freshwater wetlands, Earth system
science data, 13, 3607–3689, 2021.

495 Dewitte, S. and Clerbaux, N.: Measurement of the Earth Radiation Budget at the Top of the Atmosphere—A Review, Remote Sensing, 9,
https://doi.org/10.3390/rs9111143, 2017.

Donlon, C., Berruti, B., Mecklenberg, S., Nieke, J., Rebhan, H., Klein, U., Buongiorno, A., Mavrocordatos, C., Frerick, J., Seitz, B., Goryl,
P., Féménias, P., Stroede, J., and Sciarra, R.: The Sentinel-3 Mission: Overview and status, in: 2012 IEEE International Geoscience and
Remote Sensing Symposium, pp. 1711–1714, https://doi.org/10.1109/IGARSS.2012.6351194, 2012.

500 Driemel, A., Augustine, J., Behrens, K., Colle, S., Cox, C., Cuevas-Agulló, E., Denn, F. M., Duprat, T., Fukuda, M., Grobe, H., et al.: Baseline
Surface Radiation Network (BSRN): structure and data description (1992–2017), Earth System Science Data, 10, 1491–1501, 2018.

Faroux, S., Kaptué Tchuenté, A., Roujean, J.-L., Masson, V., Martin, E., and Moigne, P. L.: ECOCLIMAP-II/Europe: A twofold database of
ecosystems and surface parameters at 1 km resolution based on satellite information for use in land surface, meteorological and climate
models, Geoscientific Model Development, 6, 563–582, 2013.

505 Geiger, B., Carrer, D., Franchisteguy, L., Roujean, J.-L., and Meurey, C.: Land surface albedo derived on a daily basis from Meteosat Second
Generation observations, IEEE Transactions on Geoscience and Remote Sensing, 46, 3841–3856, 2008.

Ghent, D., Corlett, G., Göttsche, F.-M., and Remedios, J.: Global land surface temperature from the along-track scanning radiometers, Journal
of Geophysical Research: Atmospheres, 122, 12–167, 2017.

Ghilain, N.: Chapter 16 - Continental Scale Monitoring of Subdaily and Daily Evapotranspiration Enhanced by the Assimilation of Surface Soil Moisture Derived from Thermal Infrared Geostationary Data, in: Satellite Soil Moisture Retrieval, edited by Srivastava, P. K., Petropoulos, G. P., and Kerr, Y. H., pp. 309–332, Elsevier, https://doi.org/https://doi.org/10.1016/B978-0-12-803388-3.00016-4, 2016.

Ghilain, N., Arboleda, A., Barrios, J., and Gellens-Meulenberghs, F.: Water interception by canopies for remote sensing based evapotranspiration models, International Journal of Remote Sensing, 41, 2934–2945, 2020.

Göttsche, F.-M., Olesen, F., and Bork-Unkelbach, A.: Validation of land surface temperature derived from MSG/SEVIRI with in situ measurements at Gobabeb, Namibia, International Journal of Remote Sensing, https://doi.org/10.1080/01431161.2012.716539, 2013.

Göttsche, F.-M., Olesen, F., Trigo, I., Bork-Unkelbach, A., and Martin, M.: Long Term Validation of Land Surface Temperature Retrieved from MSG/SEVIRI with Continuous in-Situ Measurements in Africa, Remote Sensing, 8, 410, https://doi.org/10.3390/rs8050410, 2016.

Heiskanen, J., Brümmer, C., Buchmann, N., Calfapietra, C., Chen, H., Gielen, B., Gkritzalis, T., Hammer, S., Hartman, S., Herbst, M., et al.: The Integrated Carbon Observation System in Europe, Bulletin of the American Meteorological Society, pp. 1–54, 2021.

Jia, A., Liang, S., Jiang, B., Zhang, X., and Wang, G.: Comprehensive Assessment of Global Surface Net Radiation Products and Uncertainty Analysis, Journal of Geophysical Research: Atmospheres, 123, 1970–1989, https://doi.org/https://doi.org/10.1002/2017JD027903, 2018.

Jia, A., Liang, S., and Wang, D.: Generating a 2-km, all-sky, hourly land surface temperature product from Advanced Baseline Imager data, Remote Sensing of Environment, 278, 113 105, 2022.

Jia, A., Liang, S., Wang, D., Ma, L., Wang, Z., and Xu, S.: Global hourly, 5 km, all-sky land surface temperature data from 2011 to 2021 based on integrating geostationary and polar-orbiting satellite data, Earth System Science Data, 15, 869–895, 2023.

Jiang, B., Liang, S., Ma, H., Zhang, X., Xiao, Z., Zhao, X., Jia, K., Yao, Y., and Jia, A.: GLASS daytime all-wave net radiation product: Algorithm development and preliminary validation, Remote Sensing, 8, 222, 2016.

Jiang, B., Liang, S., Jia, A., Xu, J., Zhang, X., Xiao, Z., Zhao, X., Jia, K., and Yao, Y.: Validation of the surface daytime net radiation product from version 4.0 GLASS product suite, IEEE Geoscience and Remote Sensing Letters, 16, 509–513, 2018.

Jiang, B., Han, J., Liang, H., Liang, S., Yin, X., Peng, J., He, T., and Ma, Y.: The Hi-GLASS all-wave daily net radiation product: Algorithm and product validation, Science of Remote Sensing, 7, 100 080, https://doi.org/https://doi.org/10.1016/j.srs.2023.100080, 2023.

Kato, S., Rose, F. G., Rutan, D. A., Thorsen, T. J., Loeb, N. G., Doelling, D. R., Huang, X., Smith, W. L., Su, W., and Ham, S.-H.: Surface Irradiances of Edition 4.0 Clouds and the Earth's Radiant Energy System (CERES) Energy Balanced and Filled (EBAF) Data Product, Journal of Climate, 31, 4501 – 4527, https://doi.org/10.1175/JCLI-D-17-0523.1, 2018.

Köppen, W. and Geiger, R.: Handbuch der klimatologie, vol. 1, Gebrüder Borntraeger Berlin, 1936.

Lopes, F. M., Dutra, E., and Trigo, I. F.: Integrating Reanalysis and Satellite Cloud Information to Estimate Surface Downward Long-Wave Radiation, Remote Sensing, 14, https://doi.org/10.3390/rs14071704, 2022.

Maes, W. and Steppe, K.: Estimating evapotranspiration and drought stress with ground-based thermal remote sensing in agriculture: a review, Journal of Experimental Botany, 63, 4671–4712, 2012.

Martens, B., Miralles, D. G., Lievens, H., Van Der Schalie, R., De Jeu, R. A., Fernández-Prieto, D., Beck, H. E., Dorigo, W. A., and Verhoest, N. E.: GLEAM v3: Satellite-based land evaporation and root-zone soil moisture, Geoscientific Model Development, 10, 1903–1925, 2017.

Martins, J., Trigo, I. F., Ghilain, N., Jimenez, C., Göttsche, F.-M., Ermida, S. L., Olesen, F.-S., Gellens-Meulenberghs, F., and Arboleda, A.: An all-weather land surface temperature product based on MSG/SEVIRI observations, Remote Sensing, 11, 3044, 2019.

Muñoz-Sabater, J., Dutra, E., Agustí-Panareda, A., Albergel, C., Arduini, G., Balsamo, G., Boussetta, S., Choulga, M., Harrigan, S., Hersbach, H., et al.: ERA5-Land: A state-of-the-art global reanalysis dataset for land applications, Earth System Science Data, 13, 4349–4383, 2021.

Nie, J., Ren, H., Zheng, Y., Ghent, D., and Tansey, K.: Land Surface Temperature and Emissivity Retrieval From Night-time Middle-Infrared and Thermal-Infrared Sentinel-3 Images, IEEE Geoscience and Remote Sensing Letters, 18, 915–919, https://doi.org/10.1109/LGRS.2020.2986326, 2021.

550 Peres, L. F. and DaCamara, C. C.: Emissivity maps to retrieve land-surface temperature from MSG/SEVIRI, IEEE Transactions on Geoscience and Remote Sensing, 43, 1834–1844, 2005.

Poyatos, R., Granda, V., Flo, V., Adams, M. A., Adorján, B., Aguadé, D., Aidar, M. P. M., Allen, S., Alvarado-Barrientos, M. S., Anderson-Teixeira, K. J., Aparecido, L. M., Arain, M. A., Aranda, I., Asbjornsen, H., Baxter, R., Beamesderfer, E., Berry, Z. C., Berveiller, D., Blakely, B., Boggs, J., Bohrer, G., Bolstad, P. V., Bonal, D., Bracho, R., Brito, P., Brodeur, J., Casanoves, F., Chave, J., Chen, H., Cisneros,
555 C., Clark, K., Cremonese, E., Dang, H., David, J. S., David, T. S., Delpierre, N., Desai, A. R., Do, F. C., Dohnal, M., Domec, J.-C., Dzikiti, S., Edgar, C., Eichstaedt, R., El-Madany, T. S., Elbers, J., Eller, C. B., Euskirchen, E. S., Ewers, B., Fonti, P., Forner, A., Forrester, D. I., Freitas, H. C., Galvagno, M., Garcia-Tejera, O., Ghimire, C. P., Gimeno, T. E., Grace, J., Granier, A., Griebel, A., Guangyu, Y., Gush, M. B., Hanson, P. J., Hasselquist, N. J., Heinrich, I., Hernandez-Santana, V., Herrmann, V., Hölttä, T., Holwerda, F., Irvine, J., Isarangkool Na Ayutthaya, S., Jarvis, P. G., Jochheim, H., Joly, C. A., Kaplick, J., Kim, H. S., Klemedtsson, L., Kropp, H., Lagergren,
560 F., Lane, P., Lang, P., Lapenas, A., Lechuga, V., Lee, M., Leuschner, C., Limousin, J.-M., Linares, J. C., Linderson, M.-L., Lindroth, A., Llorens, P., López-Bernal, A., Loranty, M. M., Lüttschwager, D., Macinnis-Ng, C., Maréchaux, I., Martin, T. A., Matheny, A., McDowell, N., McMahon, S., Meir, P., Mészáros, I., Migliavacca, M., Mitchell, P., Mölder, M., Montagnani, L., Moore, G. W., Nakada, R., Niu, F., Nolan, R. H., Norby, R., Novick, K., Oberhuber, W., Obojes, N., Oishi, A. C., Oliveira, R. S., Oren, R., Ourcival, J.-M., Paljakka, T., Perez-Priego, O., Peri, P. L., Peters, R. L., Pfautsch, S., Pockman, W. T., Preisler, Y., Rascher, K., Robinson, G., Rocha, H., Rocheteau, A., Röll,
565 A., Rosado, B. H. P., Rowland, L., Rubtsov, A. V., Sabaté, S., Salmon, Y., Salomón, R. L., Sánchez-Costa, E., Schäfer, K. V. R., Schuldt, B., Shashkin, A., Stahl, C., Stojanović, M., Suárez, J. C., Sun, G., Szatniewska, J., Tatarinov, F., Tesař, M., Thomas, F. M., Tor-ngern, P., Urban, J., Valladares, F., van der Tol, C., van Meerveld, I., Varlagin, A., Voigt, H., Warren, J., Werner, C., Werner, W., Wieser, G., Wingate, L., Wullschleger, S., Yi, K., Zweifel, R., Steppe, K., Mencuccini, M., and Martínez-Vilalta, J.: Global transpiration data from sap flow measurements: the SAPFLUXNET database, Earth System Science Data, 13, 2607–2649, https://doi.org/10.5194/essd-13-2607-2021,
570 2021.

Pérez-Planells, L., Niclòs, R., Puchades, J., Coll, C., Göttsche, F.-M., Valiente, J. A., Valor, E., and Galve, J. M.: Validation of Sentinel-3 SLSTR Land Surface Temperature Retrieved by the Operational Product and Comparison with Explicitly Emissivity-Dependent Algorithms, Remote Sensing, 13, https://doi.org/10.3390/rs13112228, 2021.

Rains, D.: LSTRAD, https://doi.org/10.5281/zenodo.8332128, 2023a.

575 Rains, D.: LSTRAD, https://doi.org/10.5281/zenodo.8332222, 2023b.

Roerink, G., Bojanowski, J., de Wit, A., Eerens, H., Supit, I., Leo, O., and Boogaard, H.: Evaluation of MSG-derived global radiation estimates for application in a regional crop model, Agricultural and Forest Meteorology, 160, 36–47, https://doi.org/https://doi.org/10.1016/j.agrformet.2012.02.006, 2012.

Shiff, S., Helman, D., and Lensky, I. M.: Worldwide continuous gap-filled MODIS land surface temperature dataset, Scientific Data, 8, 74,
580 2021.

Stephens, G. L., Li, J., Wild, M., Clayson, C. A., Loeb, N., Kato, S., L'ecuyer, T., Stackhouse, P. W., Lebsock, M., and Andrews, T.: An update on Earth's energy balance in light of the latest global observations, Nature Geoscience, 5, 691–696, 2012.

Trigo, I. F., Monteiro, I. T., Olesen, F., and Kabsch, E.: An assessment of remotely sensed land surface temperature, Journal of Geophysical Research: Atmospheres, 113, 2008a.

585 Trigo, I. F., Peres, L. F., DaCamara, C. C., and Freitas, S. C.: Thermal land surface emissivity retrieved from SEVIRI/Meteosat, IEEE Transactions on Geoscience and Remote Sensing, 46, 307–315, 2008b.

Trigo, I. F., Barroso, C., Viterbo, P., Freitas, S. C., and Monteiro, I. T.: Estimation of downward long-wave radiation at the surface combining remotely sensed data and NWP data, Journal of Geophysical Research: Atmospheres, 115, 2010.

Trigo, I. F., Dacamara, C. C., Viterbo, P., Roujean, J.-L., Olesen, F., Barroso, C., Camacho-de Coca, F., Carrer, D., Freitas, S. C., García-Haro,
590 J., et al.: The satellite application facility for land surface analysis, International Journal of Remote Sensing, 32, 2725–2744, 2011.

Trigo, I. F., Ermida, S. L., Martins, J. P., Gouveia, C. M., Göttsche, F.-M., and Freitas, S. C.: Validation and consistency assessment of land surface temperature from geostationary and polar orbit platforms: SEVIRI/MSG and AVHRR/Metop, ISPRS Journal of Photogrammetry and Remote Sensing, 175, 282–297, https://doi.org/https://doi.org/10.1016/j.isprsjprs.2021.03.013, 2021.

Verma, M., Fisher, J. B., Mallick, K., Ryu, Y., Kobayashi, H., Guillaume, A., Moore, G., Ramakrishnan, L., Hendrix, V., Wolf, S., Sikka, M.,
595 Kiely, G., Wohlfahrt, G., Gielen, B., Roupsard, O., Toscano, P., Arain, A., and Cescatti, A.: Global Surface Net-Radiation at 5 km from MODIS Terra, Remote Sensing, 8, https://doi.org/10.3390/rs8090739, 2016.

Wielicki, B. A., Barkstrom, B. R., Harrison, E. F., Lee III, R. B., Smith, G. L., and Cooper, J. E.: Clouds and the Earth's Radiant Energy System (CERES): An earth observing system experiment, Bulletin of the American Meteorological Society, 77, 853–868, 1996.

Wu, Z., Teng, H., Chen, H., Han, L., and Chen, L.: Reconstruction of Gap-Free Land Surface Temperature at a 100 m Spatial Resolution
600 from Multidimensional Data: A Case in Wuhan, China, Sensors, 23, 913, 2023.

Xu, J., Liang, S., and Jiang, B.: A global long-term (1981–2019) daily land surface radiation budget product from AVHRR satellite data using a residual convolutional neural network, Earth System Science Data, 14, 2315–2341, 2022.

Xu, S. and Cheng, J.: A new land surface temperature fusion strategy based on cumulative distribution function matching and multiresolution Kalman filtering, Remote Sensing of Environment, 254, 112 256, 2021.

605 Young, A. H., Knapp, K. R., Inamdar, A., Hankins, W., and Rossow, W. B.: The international satellite cloud climatology project H-Series climate data record product, Earth System Science Data, 10, 583–593, 2018.

Zheng, Y., Ren, H., Guo, J., Ghent, D., Tansey, K., Hu, X., Nie, J., and Chen, S.: Land surface temperature retrieval from sentinel-3A sea and land surface temperature radiometer, using a split-window algorithm, Remote Sensing, 11, 650, 2019.